Muli-Frequency Cable Vibration Experiments

by

Andrew Wiggins

Submitted to the Department of Ocean Engineering
in partial fulfillment of the requirements for the degree of

Master of Science in Ocean Engineering

at the

MASSACHUSETTS INSTITUTE OF TECHNOLOGY

June 2005

Author ....
Department of Ocean Engineering
May 18, 2005

Certified by ....
Michael S. Triantafyllou
Professor, Department of Mechanical and Ocean Engineering
Thesis Supervisor

Accepted by ....
Michael S. Triantafyllou
Director of the Center for Ocean Engineering

Muli-Frequency Cable Vibration Experiments

by

Andrew Wiggins

Submitted to the Department of Ocean Engineering
on May 18, 2005, in partial fulfillment of the
requirements for the degree of
Master of Science in Ocean Engineering

Abstract

A series of Multi-Frequency cable vibration experiments at Reynolds number 7600 were carried out at the MIT Tow Tank using the Virtual Cable Towing Apparatus (VCTA). Motions observed in a Direct Numerical Simulation of a flexible cylinder in a shear current were imposed on the VCTA and force measurements taken. Results showed a good agreement between the RMS lift coefficients of experiment and simulation. Complex Demodulation Analysis revealed significant lift force phase modulations. This analysis also showed that to a large extent the 3-dimensional behavior of the DNS was captured by the 2-d experiment in regions of low inflow, and to a lesser extent in regions of high inflow. Applications of results to future vortex induced vibration force models are discussed.

Thesis Supervisor: Michael S. Triantafyllou
Title: Professor, Department of Mechanical and Ocean Engineering

Acknowledgments

First of all I would like to thank my sponsor for the opportunity to explore the rich problem of cable vibrations. Secondly, I'd like to thank my supervisors Professor Michael S. Triantafyllou and Dr. Franz. Hover. They have been exceedingly patient with this project and have served as a veritable fountain of ideas. I'd also like to acknowledge my predecessors at the tow tank who helped develop and refine the VCTA apparatus. Without their work, this thesis would not have been possible. Lastly, I'd like to thank fellow students Jason Dahl and Didier Lucor and my supportive parents.

Contents

List of Figures

List of Tables

Nomenclature

D	Cylinder diameter
F_L	Lift force
F_d	Drag force
f_e	Forcing frequency
L	Cylinder length
ρ	Fluid Density
U_{exp}	Carriage Velocity
U_x	Local Inflow Velocity in Simulation
Y	Heave Position
z	Spanwise Position
ϕ	Phase between force and motion
∇	Volume of cylinder
$(\frac{Y}{D})$	Amplitude Ratio
σ	Standard Deviation
$C_D = \frac{F_d}{.5\rho U_{exp}^2 LD}$	Drag force coefficient
$C_L = \frac{F_L}{.5\rho U_{exp}^2 LD}$	Lift force coefficient
C_{LV}	Lift force coefficient in phase with velocity, defined in chapter 3
C_{LA}	Lift force coefficient in phase with acceleration, defined in chapter 3
C_m	Added mass coefficient
$f_r = \frac{f_e D}{U_{exp}}$	Reduced Frequency
$V_r = \frac{1}{f_r}$	Reduced velocity

Chapter 1

Introduction

1.1 Motivation

The ability to accurately model the vortex-induced vibration (VIV) of structures is of a practical interest to engineers in a variety of fields. In structures diverse as heat exchanger tubes, chimney stacks and suspension bridges, VIV can govern fatigue life, global loads and affect performance. Perhaps the most important cases of VIV occur in the ocean, where vortex shedding regularly causes high frequency oscillations of riser tubes and marine cables. Exposed to highly sheared flows, these high-aspect ratio structures are particularly susceptible to VIV and pose unique challenges for the engineer.

The phenomenon of VIV itself has been observed for centuries. Harnessing the power of VIV, King David for instance would place his guitar above his bed such that the breeze would excite the strings [1, pp. 11]. It was actually Leonardo Da Vinci who first identified the physical mechanism behind VIV when he sketched the vortex wake pattern he observed behind a bluff body in a river [1, pp. 11]. However, it isn't until the early twentieth century with the work of Benard that these vibrations are linked to vortex shedding [9, pp. 15].

The years surrounding the turn of the century was a particularly formative period for VIV research. It was in this period that Strouhal discovered the fundamental relation between the vortex shedding frequency, a body's characteristic diameter and the free stream velocity (see Figure 1-3). A little later, while working on cylindrical biplane spars, Theodore von Karman would discover the alternating vortex pattern that now bears his name (see Figure 1-4).

VIV is a complex problem, where structural properties, the inflow velocity profile, roughness, and viscosity all come into play in a fundamentally nonlinear manner. This complexity leads to difficult experiments and very high computational costs at the scales of interest. Progress has been made in solving the fully nonlinear problem, both by experiment and simulation (see [14]-[13]),but for the majority of practical applications simplifying assumptions have to be made.

One of simplifying assumptions often made is that the the flow is locally two-dimensional and that the forces on the cylinder may be approximated by a strip theory approach. The aim of this thesis is to see to what extent the true three-dimensional behavior is captured in a two-dimensional approximation. To accomplish this, experiments were conducted in the MIT Tow Tank and compared with the the non-linear DNS studies of Didier and Karniadakis [14]. In addition, the sensitivity of the response to Reynolds number was also examined.

This introduction continues with a discussion of the VIV response in various flow regimes.

Chapter two describes the methodology used in these experiments.

Chapter three presents some of the novel post processing techniques used in the study.

Chapter four summarizes the results of the experiments and offers conclusions and recommendations for future work.

1.2 The VIV Phenomenon

1.2.1 Stationary Cylinder

As pointed out by Leonardo, the wake of a bluff body [1] is characterized by vortex shedding. Unlike the potential flow solution to the flow around a cylinder, the pressure distribution around a bluff body such as cylinder in real fluid is not fore/aft symmetric and full pressure recovery does not take place. Consequently, there is a net drag force on the object. Additionally, the boundary layer is no longer being forced onto the body and detaches, forming a shear layer. On a cylinder, or around a sphere as in Figure 1-1 the separation occurs near the widest part of the body. The exact location of separation, like the wake pattern itself, is a function of the Reynolds number. Figure 1-1 also clearly shows the shear layers rolling inward.

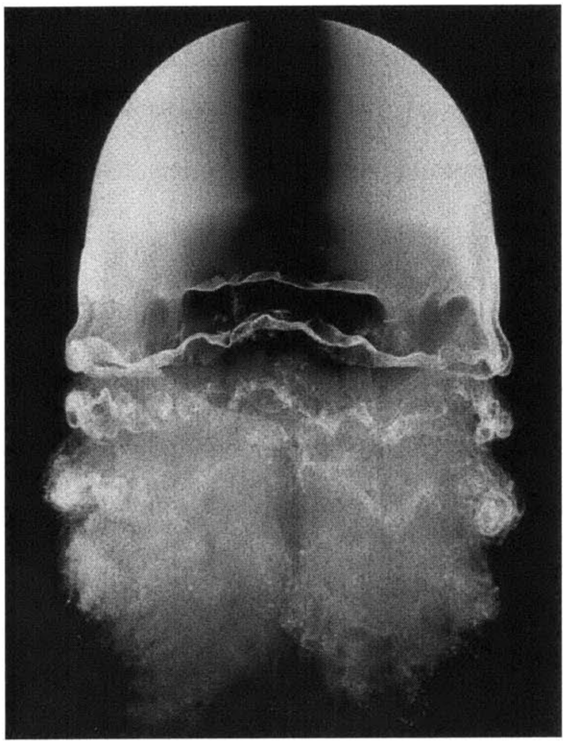

Figure 1-1: Flow Separation[25]

Figure 1-2 charts the effect of viscosity on the wake pattern behind a stationary

---

[1] A "bluff body" is any body where the flow separates from a "large" potion of the surface

cylinder. At a Reynold number (RE) of around 40, vortices start to appear. These are caused by the velocity gradient and instability in the wake. Above RE = 40, the celebrated *von Karman vortex street* is formed. Two opposite signed vortice are generated and convected downstream. Accompanying the *von Karman street* is a periodic force on the cylinder. This is caused by the fact that induced velocities from the vortices in the near wake alter the pressure distribution on the cylinder. Integrating the pressure, it is found that there is both an alternating drag force and lift force: the drag force occurring at a frequency twice that of the lift force. The induced velocity due to near wake vortex also influences boundary layer development and nearby vortices. More detailed descriptions of the vortex shedding process can be found in Sarpkaya [19] and Williamson & Roshko[26].

The experiments in this study were performed at $1000 < RE < 20000$, placing them in the so-called "subcritical" regime. In this regime, the wake is fairly organized and the frequency of shedding is surprisingly well-defined. The boundary is laminar up till the separation point. Figure 1-3 shows that the Strouhal number is approximately 0.2 for the Reynolds number range of the experiment. Strouhal Number is defined in Nomenclature section.

In the "transition" regime, at RE above $3x10^5$, the wake becomes less organized, drag decreases and the shedding frequency becomes variable and sensitive to surface roughness. The wake width also decreases.

Moving to RE beyond the transition region, Roshko [26] has found that the wake returns to a fully turbulent von Karman street type wake. The drag coefficient increases.

1.2.2 Flexible Cylinder

Thus far, only the case of a stationary cylinder has been considered. It isn't too much of a stretch however to envision a case where the periodic forces due to the vortices are sufficient to excite the structure. The problem then becomes one of fluid/structure interaction, the velocity at the body no longer being simply the free stream velocity but the vector sum of the free stream and the body motion.

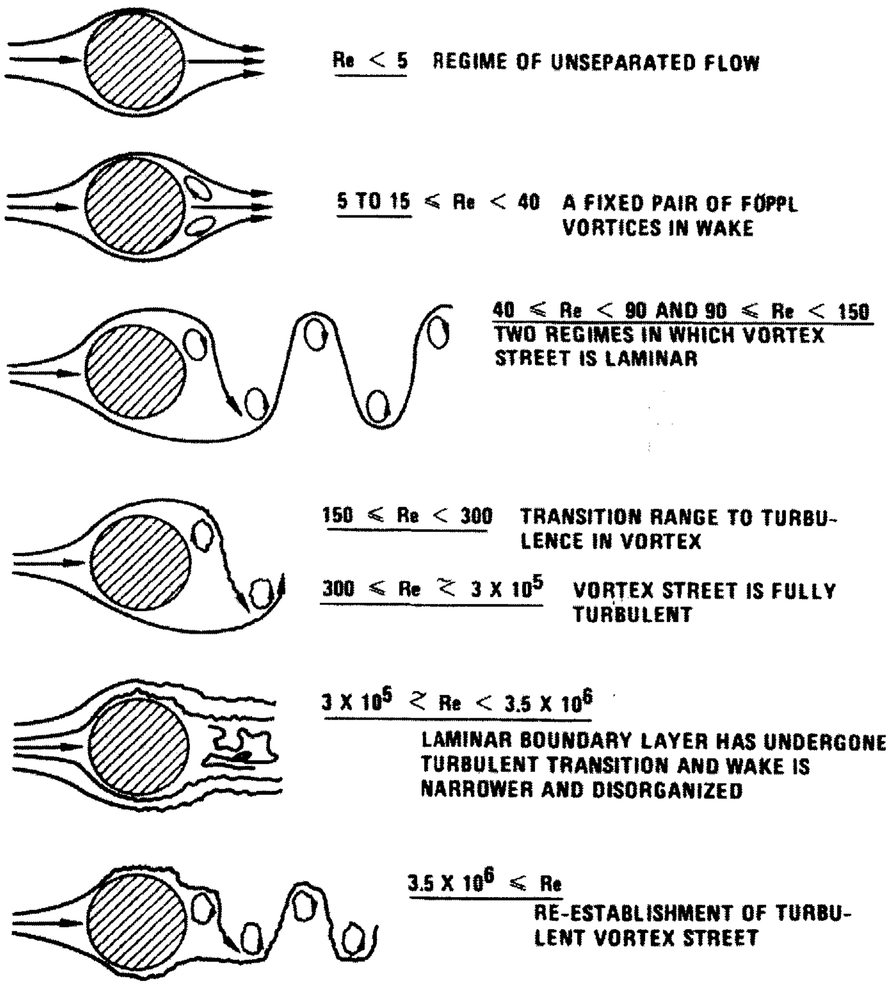

Figure 1-2: Fixed Cylinder Wake Patterns at various Flow Conditions

In addition to being a function of Reynolds number, the wake pattern for the compliant cylinder is also a function the motion amplitude and vibration frequency. This can be seen in Figure 1-4. The abscissa of this graph is the reduced velocity, and the ordinate is the motion amplitude divided by the diameter The "2S" of this chart represents the same von Karman type street wake seen for the stationary cylinder. The "2P" wake pattern however is something altogether different. The "2P" pattern is characterized by two pairs of vortices being shed with each motion reversal. The presence of unstable vortex shedding patterns such as "P+S" indicates that the observations of 1-4 were made from a forced vibration experiment, as vortex shedding

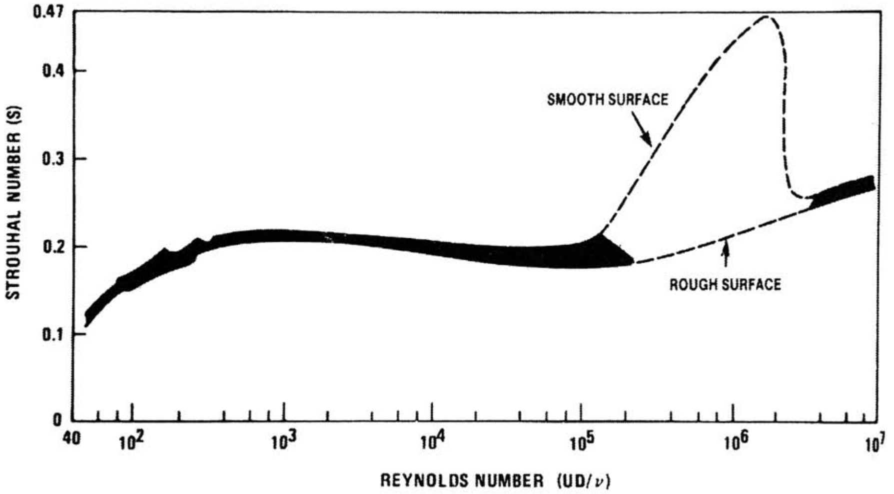

Figure 1-3: Strouhal Number as a function of Reynold Number

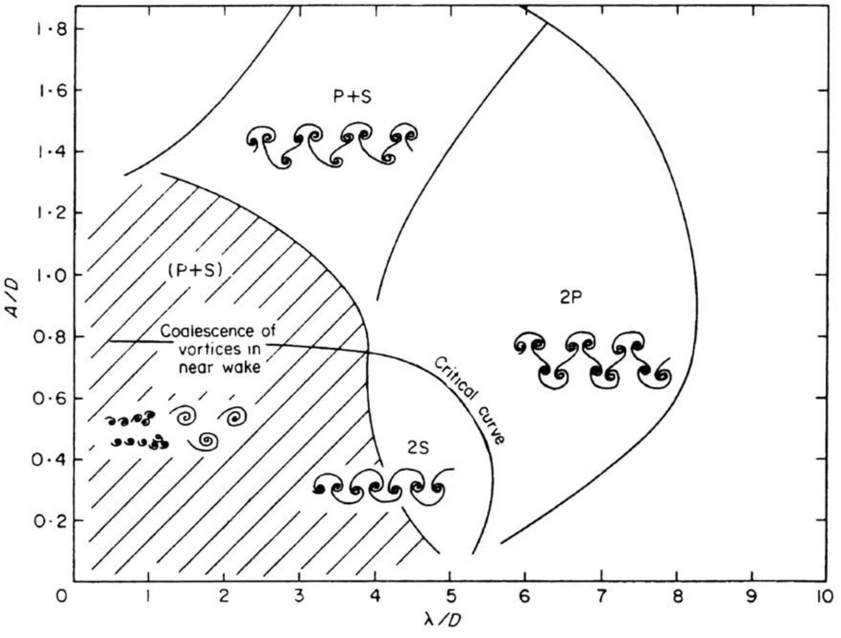

Figure 1-4: Transition in Shedding Patterns

patterns such as "P+S" have not been observed to induce free vibration. The bounds of stable wake patterns indicate that VIV motions for a symmetric body such as a cylinder are self-limiting.[1, pp. 22].

Near a $V_{RN} = 5$ (corresponding to a Strouhal Number of 0.2), there is a distinct change of shedding modes. This change of modes is one of the defining defining features of flexible cylinder vibrations. "Lock-in", as it is known, occurs when the vortex shedding frequency synchronizes with the frequency of the vibrating cylinder. "Lock-in" is characterized by a wide peak in the response spectra. Oscillations, in excess of 1.4 diameters have been observed in the lock-in region.

The classic results of Feng [1, 24] illustrate the lock-in phenomenon well. We see that the frequency of shedding satisfies the Strouhal relation up until $V_{rn} = 5$, at which point the frequency of shedding collapses onto the natural frequency of the structure. This collapse arises from the competition between the natural Strouhal shedding mode and the one introduced with the body motion.

There are two distinct regions within the lock-in band of frequencies. In the lower reduced velocity half of the lock-in region, energy from the near wake is input into the structure, indicated by a positive value of C_{LV}(see Nomenclature and the section on Post processing for more explanation of C_{LV}). The vortex shedding frequency is lower than the natural stationary cylinder shedding frequency. The added mass is usually larger than the potential flow value of one in this region.

As the reduced velocity is increased, a critical V_{rn} is eventually reached. Recent work by Krishanmoorthy [12] has shown that at this at the critical velocity the wake is bistable and will change states almost periodically between 2S and 2P type vortex formations over a couple of cycles. The phase between fluid force and motion will behave in a similarly erratic manner. Above the critical reduced velocity, damping occurs as the shedding process is driven by the structure. The added mass coefficient is usually less than one in this region.

Experiments have shown that the shape of the motion response curve (shows below in Figure 1-5) is determined by structural properties. The width of the lock-in band is heavily influenced by the structural damping[15]. The peak amplitude of motion is dependent on the structural damping and the cylinder mass ratio (see Nomenclature).

There are a number of interesting effects accompanying lock-in. Gopalkrishnan[9] and others[15] have discovered the fluctuating and mean drag force is amplified at lock-in. Flow visualization and other studies [15] have shown that at lock-in the wake

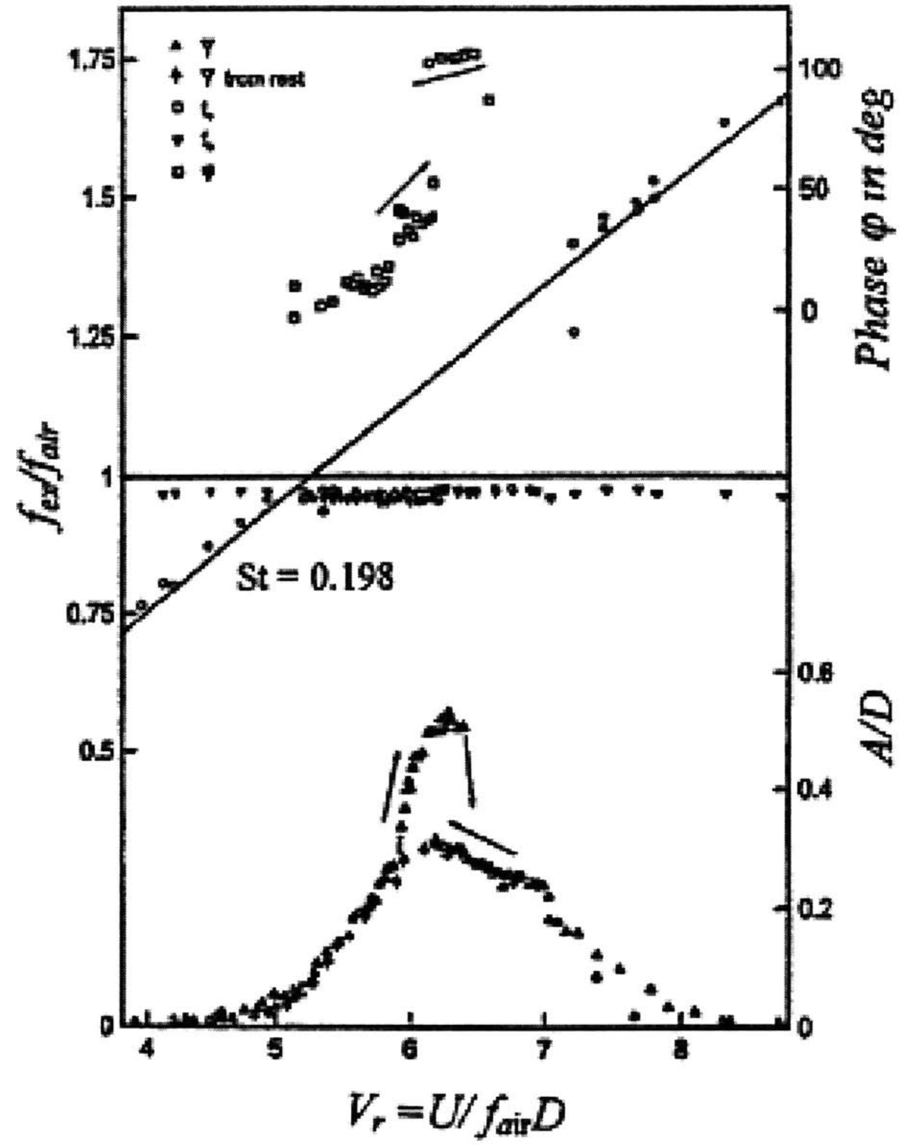

Figure 1-5: Resonance of a rigid circular cylinder with vortex shedding

becomes much more organized and the spanwise correlation of the wake increases.

One interesting side-effect of importance to our analysis is the observation by Bishop and Hassan in 1964[25] that the critical transition frequency depends on whether the frequency is being increased or decreasing. This hysteritic property could have implications in our experiments where the frequency of oscillation is a function of time.

1.2.3 A Long Flexible Cylinder in Shear Flow Conditions

Up to this point the discussion has focused on nominally two-dimensional flows, where the span of the cylinder is subjected to a uniform inflow velocity U_0. In actuality, more often than not the inflow varies with the span and transverse position, $U = f(y, z)$, where y is the transverse position and z is the spanwise coordinate. This is case of any riser in deep water waves, where the orbital velocities decay exponentially. The shear flow profile is even more extreme is places such as the Gulf of Mexico, where the orbital decay and the Gulf Stream Current combine to create highly sheared profiles such as shown in Figure 1-6.

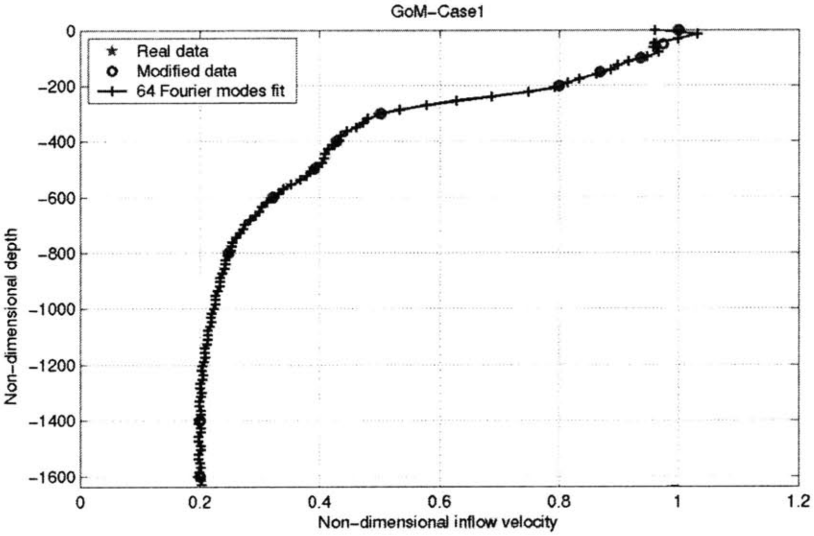

Figure 1-6: Gulf of Mexico Shear Profile

Using the insight gained in the 2-dimensional discussion of Sections 1.2.1 and 1.2.2, one can reason that given a shear profile such as Figure 1-6, different regions of the the cable may/must be locked in to different structural modes (see Figure 1-7).

The wake pattern and cylinder motion for such a case will be complicated. With varying motion frequencies, it is improbable that the entire span of a long cylinder will be correlated. Instead it is likely that correlated vortex "cells" will be shed. The interaction of these "cells" with the body and other vortices is not-trivial and requires a sophisticated coupling of the structure and fluid interactions[8]. Figure 1-8 shows

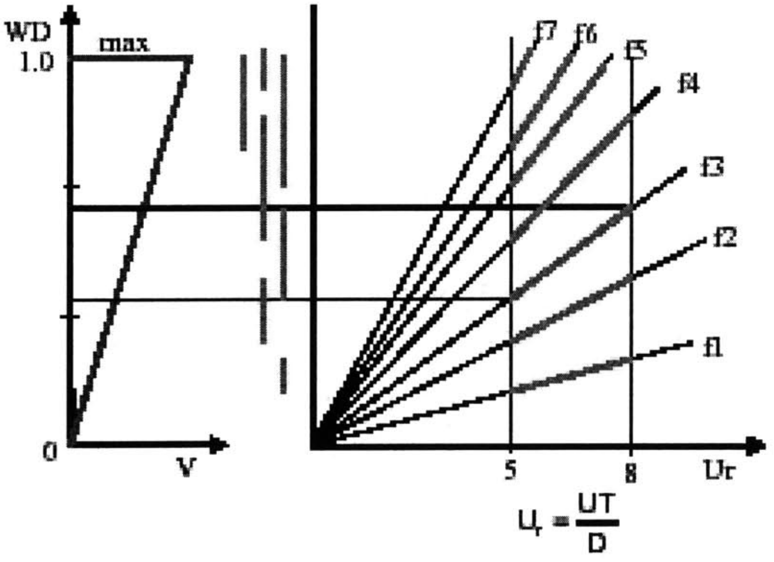

Figure 1-7: Locked In Regions

the vortex wake of one such simulation performed by George Karniadakis and Didier Lucor [14] of Brown University.

The cylinder motion under sheared flow condition will be similarly complicated. At the outset, it is unclear whether all modes that *can* be excited by a given shear flow *will* participate simultaneously. It is probable that particular modes will dominate and that transitions and interaction between modes will take place. Hydrodynamic and structural damping will play an important role in the motion evolution, causing spanwise waves to decay. Analysis shown in [14] and Chapter 3 shows that the cylinder response is often very weakly stationary.

Performing a Direct Numerical Simulation (DNS) of a long flexible cylinder in a shear flow, Karniadakis et al ([14]-[13]) observed very rich wake patterns and cable motions. The hybrid shedding mode 2S+SP and vortex splitting was seen. Their simulation also captured behavior such as the existence of standing waves, and waves traveling along the cylinder span. Being DNS, their model did not resort to a turbulence model, but was limited by computational cost/Reynolds number, as the mesh size required to resolve all energy scales in three dimensional DNS is proportional to

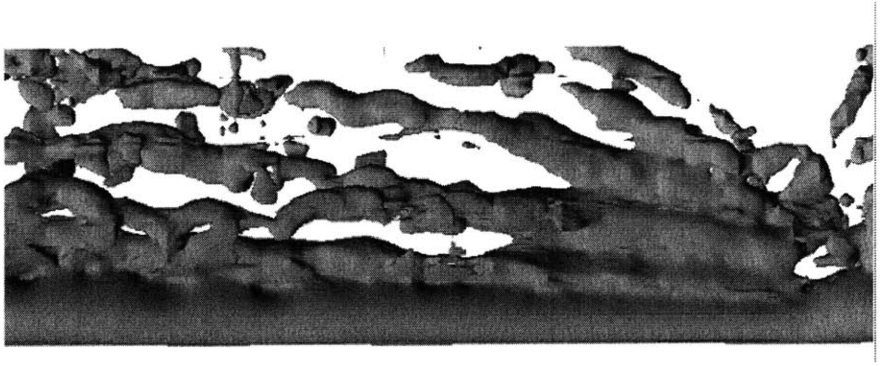

Figure 1-8: Vortex Wake [8]

$Re^{9/4}$ [6]. Thus, the simulation was carried out at moderate Reynolds Numbers between 1000-3000 using parallel processing techniques to reduce computational time. Recently, Karniadakis et. al. has done simulations of a flexible cylinder at an RE of 10000[6].

Figure 1-9 shows a typical motion history at a point along the cylinder span. This particular time series is from a point mid-span of a cylinder in an exponential inflow. The bottom velocity of the inflow is equal to 30% of the free-stream velocity. Notice the intricate nature of the motion. The simulation of Karniadakis was able to capture the presence of multi-frequency and beating patterns reported in full-scale experiments[11].

Reproduced in Figure 1-10 and 1-11 are plots of the cross-flow displacement for the whole span as a function of time. While both these cases exhibit a mixed type response, the response to a uniform inflow 1-10 is dominated by standing wave patterns. On the hand, the response to the exponential inflow, Figure 1-11 is distinguished by traveling wave (chevron patterns). It is perhaps more useful to think of the cylinder response more as a combination of standing and traveling waves than a superposition of modes 1-7.

Figure 1-12 shows the lift in phase with velocity as a function of span for a number of different shear profiles[14] (see Appendix A for the shear profiles of each case). As will be described in more detail in Chapter 3, the lift in phase with velocity is an indicator of the power flow of the system. A positive C_{LV} value indicates that power is

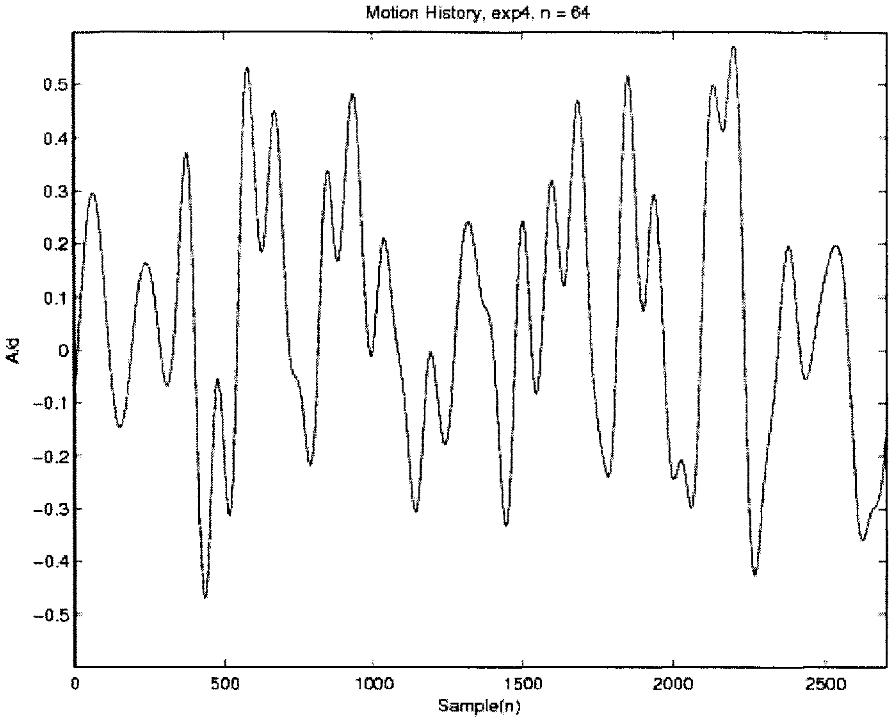

Figure 1-9: Typical Cylinder Motion History(Exponential Case)

being transferred from the fluid to the structure. As one would expect, the structure absorbs energy from the fluid at the side of the high inflow and viscous damping takes place at the side of the low inflow.

1.3 Strip Theory Approach to the Shear Flow Problem

Despite recent advances in CFD tools, the prediction of VIV response is typically carried out using semi-empirical programs such as Shear 7 and VIVA Array. These programs aim to solve the structural wave equation given hydrodynamic forcing terms. To evaluate these hydrodynamic terms, the programs usually have to rely on empirical databases of hydrodynamic coefficients such as those compiled by Gopalkrishnan [9]; the result of forced vibration tests on rigid cylinders. Figure 1-14 is a contour plot of hydrodynamic coefficients, like those used by these programs.

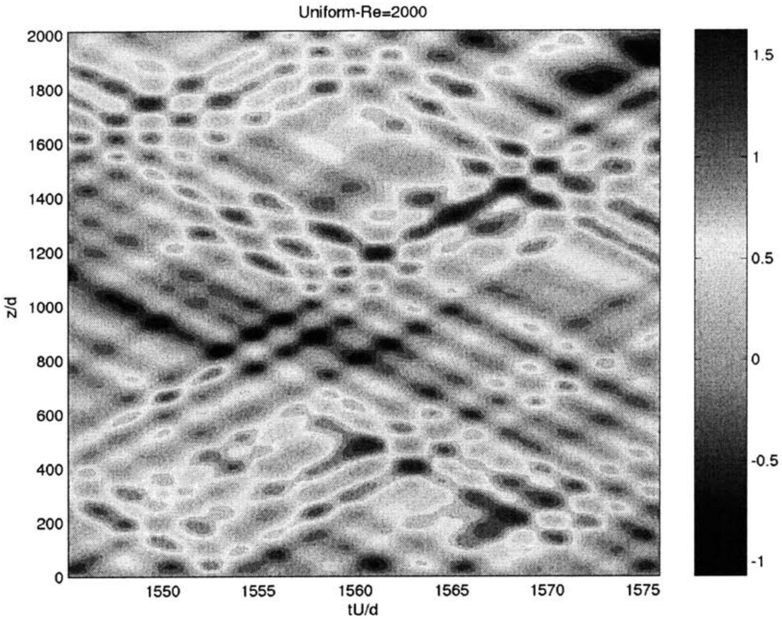

Figure 1-10: Spatio-temporal cylinder crossflow displacement (Uniform Inflow)

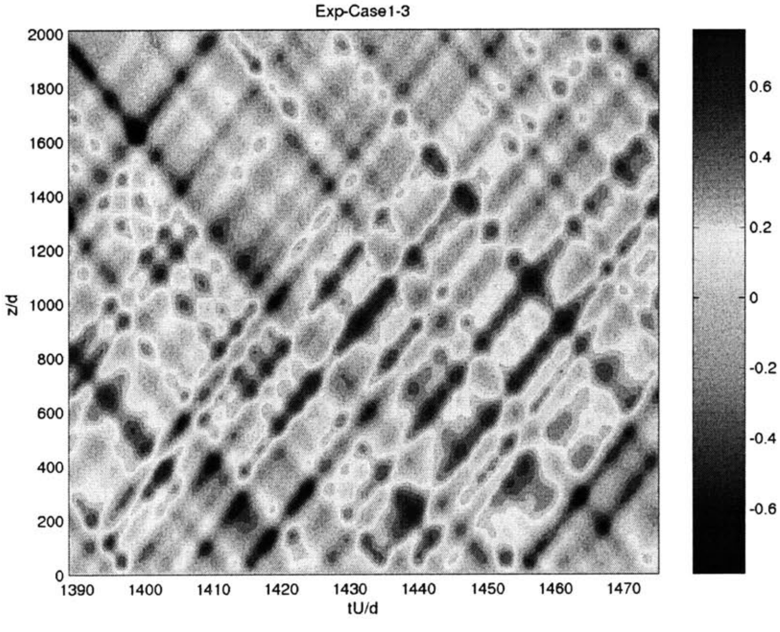

Figure 1-11: Spatio-temporal cylinder crossflow displacement (Exponential Inflow)

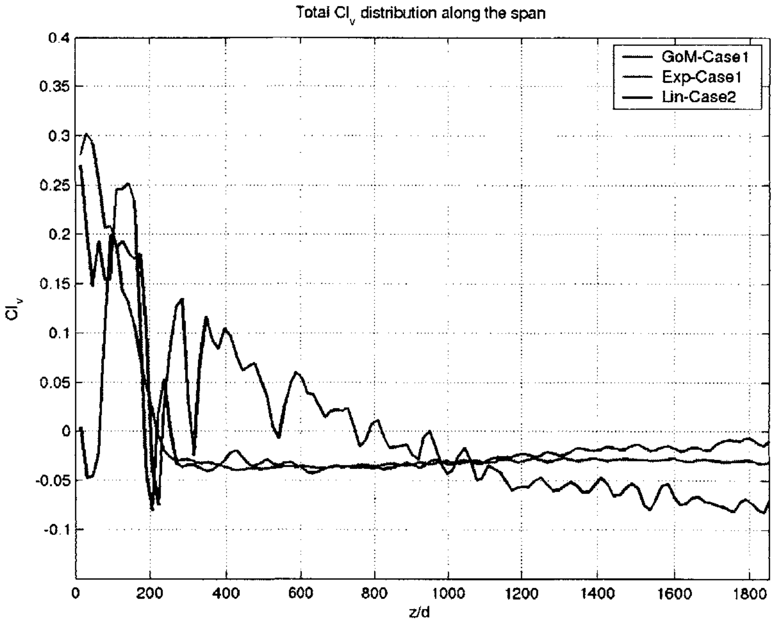

Figure 1-12: C_{LV} varying with spanwise position

Typically the structural problem is solved mode by mode in the frequency domain. Figure 1-13 from [4] shows the loading for the second mode of a riser. Similar to Figure 1-12 a certain region of the riser is excited/locked-in while damping occurs everywhere else. As the hydrodynamics coefficients are non-linear functions of amplitude and frequency, and the motion amplitudes are functions of the hydrodynamic coefficients, the problem must be solved iteratively. In this sense, the solution method the reflects the true hydroelastic nature of the VIV problem.

While each of these programs employ structural models of varying sophistication, they are all based on two key assumptions.

1. Motions in the inline direction can be neglected.

2. Fluid forces can be described locally as a non-linear oscillators

It is the validity of this second assumption that will be explored in this thesis. The first assumption is currently being examined by Jason Dahl of the MIT Tow Tank.

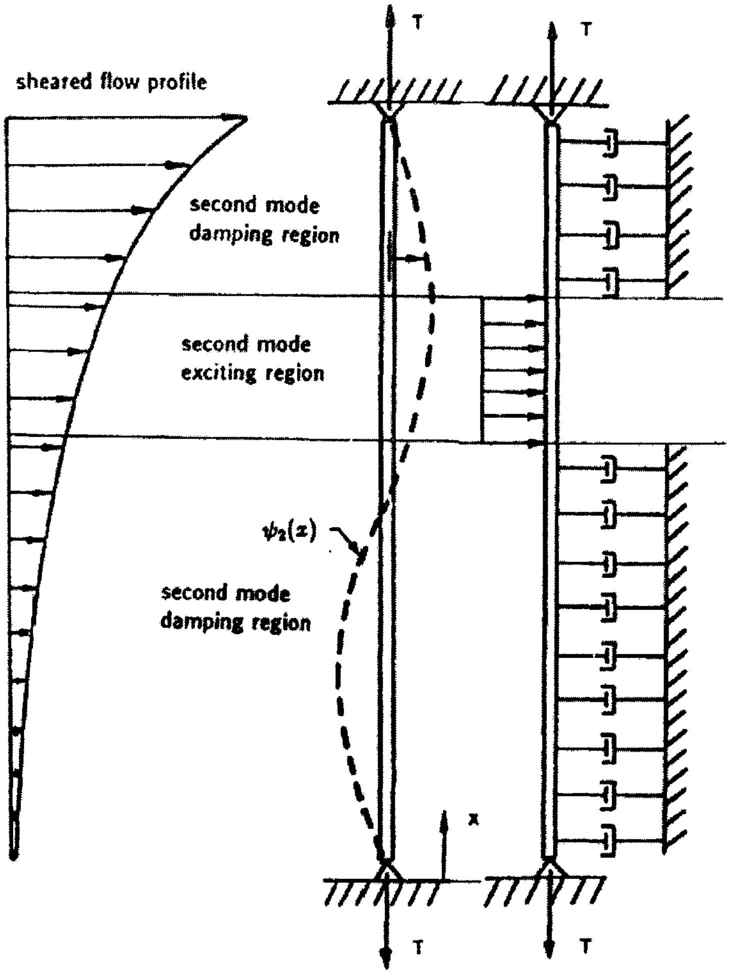

Figure 1-13: Strip Theory Approach

1.4 Previous Research at MIT and the VCTA Apparatus

There has been a great deal of experimental research done in the area of VIV at MIT. In addition to the standard run of forced and free vibration experiments [15],[5], researchers in the tow tank have investigated the behavior of tapered cylinders [23],[24], oscillating foils and various VIV suppressing devices [9].

There are two principal platforms for VIV testing in the tow tank, the Virtual

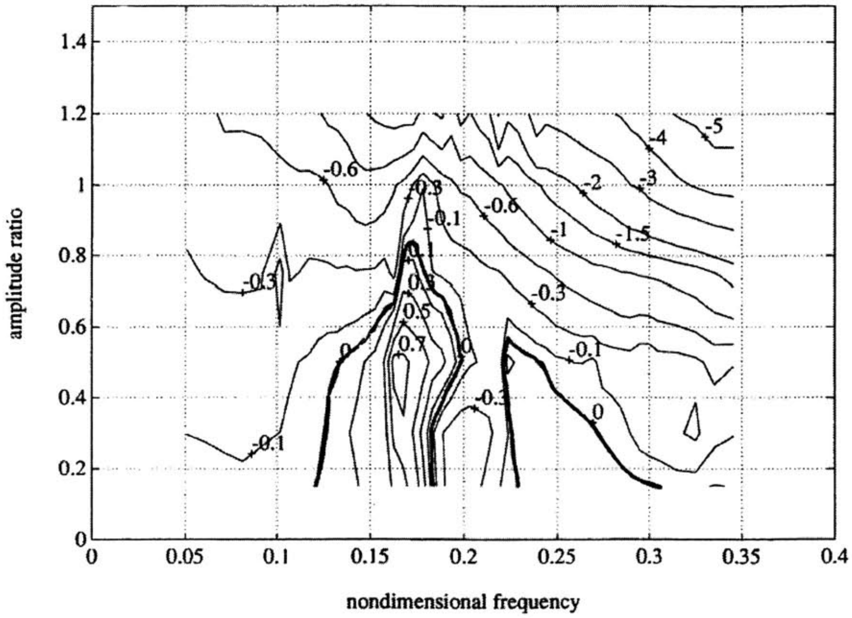

Figure 1-14: C_{LV} contours for sinusoidal oscillations [9, pp. 78]

Cable Towing Apparatus (VCTA) and the Spring Cylinder Rig (SCR). A variation on the original apparatus used by Gopalkrishnan [9] the VCTA is a versatile platform for performing VIV tests. Running a real-time simulation of free cylinder vibration, one is able to the alter the virtual structural properties of the system, achieving an almost limitless set of test configurations. A substantial upgrade of the control code on this apparatus was carried out by Oyvind Smogeli in 2002 [22].

The set-up of the VCTA can be seen in Figure 1-15, [15]. It consists of a linear table and servo drive mounted on an A-frame, capable of heaving the test cylinder at frequency up to 3 hz. The apparatus can handle test cylinders of up to 2 meters in length. Lift and drag Force measurements are obtained through piezoelectric force sensors. The amplifiers for these sensors as well as the motion control computer are located on the carriage. The vertical position of the cylinder is measured by a linear variable differential transformer (LVDT). It is this apparatus, used in the forced vibration mode that is used to carry out the experiments in this study.

The SCR is a relatively new addition to the VIV lineup at the towtank. This apparatus give us the capability to perform 2 DOF cylinder motion studies.

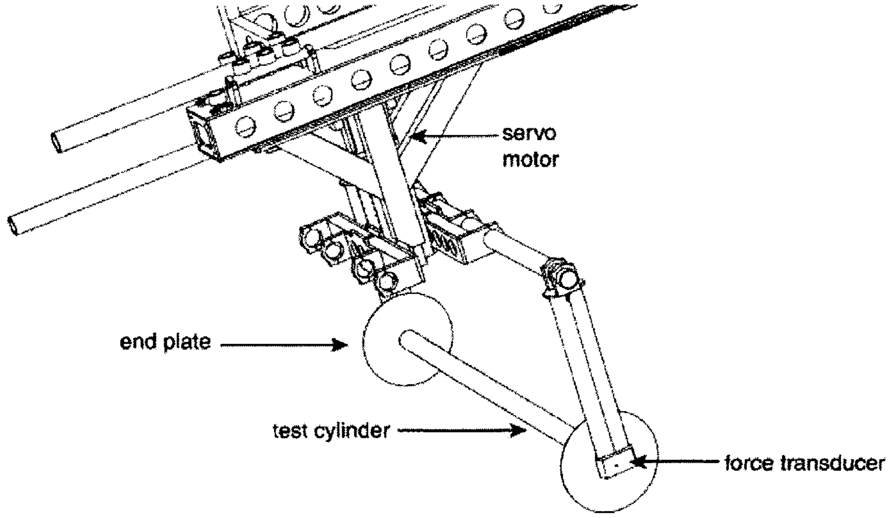

Figure 1-15: VCTA Apparatus

Chapter 2

Preparation of Experiments

2.1 Experimental Matrix

The experiments consisted of a series of tests where the the multi-frequency cylinder motion recorded by the Karniadakis et. al. [14] was imposed on the VCTA for a set shear flow profiles. A total of nine different inflow profiles were considered. For the linear and exponential profile cases three bottom velocites were investigated. We also looked at the response to shear profiles such as those found in the Gulf of Mexico (GOM), Figure 1-6.

As seen in Figure 1-9 and in the Brown group's work [8], the resulting cylinder motion in these currents is quite complicated, comprised of a number of dominant and subdominant frequencies. In this respect, the tests differed from the systematic dual-frequency experiments of Gopalkrishnan[9]. The motions imposed on the VCTA represent the "actual" motion at a single location on a flexible cylinder undergoing VIV in all but two respects. One, the Reynolds number of the simulation was lower than lower than typically experienced in the field. Secondly, the cylinder was constrained to move in cross-flow direction only. Because of this, whenever the results of the experiment are to be compared directly to the DNS, we try to get the Reynolds number as low as possible. By design a cylinder mounted on the VCTA can only heave in the cross-flow direction, and thus provided a good basis for comparison.

To go from the raw data from the simulation, a number of operations had to performed.

Proper frequency/amplitude scaling: As seen in the next section, scaling from non-dimensional time to real time has very real effects on the feasibility of carrying out experiments in the low inflow region.

Signal Blending and Concatenation: In order to maximize the effective run length and minimize transient effects in the lift measurements, a scheme for concatenating and blending the motion signals had to be developed.

Motion Control: Accurate tracking of the prescribed motion was necessary for succesful experiments. To do this, a motion program was written for the VCTA and validated.

2.2 From DNS results to Experiment

The results of the direct-numerical simulation are provided in columnar form, with non-dimensional heave position (A/d), lift and drag coefficients given as a function of non-dimensional time. (lift and drag coefficient are defined in the Nomeclature secton). Non-dimensional time t^1 is given in a form similar to the Strouhal number.

$$t^1 = \frac{tU_{max}}{D} \tag{2.1}$$

where t is the dimensional time,U_{max} is the maximum inflow velocity and D is the cylinder diameter.

Solving for t in 2.1 does not yield the time step needed for the experiment, instead a local non-dimensional time t^x,using the local inflow velocity needs to be defined, Since velocities for the simulation range from 0 to 1, where $U_{max} = 1$, the expression for the non-dimensional time at location x is simply:

$$t^x = t^1 U_x = \frac{tU_0}{D_{exp}} \tag{2.2}$$

U_x is the local inflow velocity from the simulation, U_0 is the tow speed and D_{exp} is the diameter of the test cylinder.

The implication of 2.2 for our tests is significant; for a set tow speed and test cylinder, the commanded frequency for tests in regions of low inflow has to be significantly higher than in regions of high inflow. Logically, this makes sense since the frequency of oscillation is largely controlled by the energetic high side. This can be seen in Figure 2-1, where in terms of t^1, the mean excitation frequency along the span is a relatively constant .11, with a slight decrease due to damping in the low inflow region. Recalling 2.2, one realizes that for this shear profile where $U_{min} = .1U_{max}$, the frequency in Figure 2-1 would have decrease ten fold from high to low inflow for the commanded frequency to stay the same. The upper limit of the VCTA heave frequency is around 2 hz.

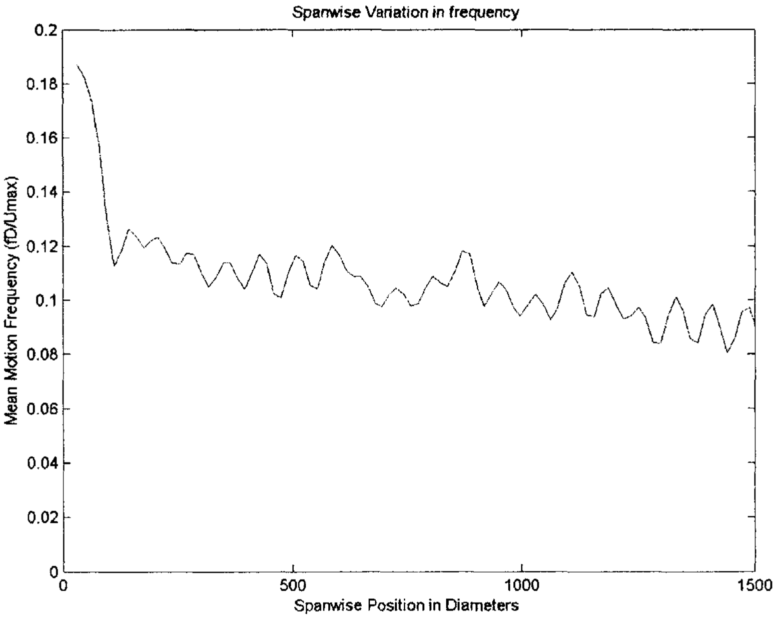

Figure 2-1: Mean frequency vs. span

Frequency scaling issues also affect the range of Reynolds numbers that can be acheived. Keeping the same test cylinder and test location, it follows from 2.2 that doubling the Reynolds number requires a doubling of the commanded frequency of motion. This means that Reynolds numbers changes are best approached by changing the cylinder diameter. Equation 2.2 poses major problems for performing high reynolds number test at location of low inflow with the current VCTA apparatus.

Correction for the local inflow velocity also have to made to the lift and drag coefficients.

2.2.1 Signal Concatenation

One result of the high computational cost of the DNS and the frequency scaling issue discussed in Section 2.2 is that in real time the commanded signals are very short. They range in length anywhere from a couple seconds for a high Reynolds number test at a low inflow velocity location to 40 seconds in length for a moderate Reynolds number test at a high-inflow velocity location. Given the short signal lengths and capabilities of the MIT tank tank, we could greatly reduce the time required for testing if we could string runs together. The only problem is that signals such as in Figure 1-9 do not naturally flow from head to tail. To overcome this, a careful blending technique was developed to ensure smooth transition between the end of one signal and the beginning of the next.

The transition from rest to motion is also important for maximizing the useful data length. The experiments showed that it takes at least a cycle for the lift signal of a cylinder starting at rest to match that of a cylinder already in motion [1]. As the signals are already very short, it is to our advantage to minimize such transient responses. Data length is especially crucial for spectral analysis where the data length influences the frequency resolution.

A number of different signal blending techniques were investigated. The first technique implemented was the "shift and blend" method illustrated in Figure 2-2. In this method,the beginning and ends of the signal are overlapped and blended into

---

[1] As you will see in the results section, the lift signals proved to be very repeatable

each other using a hyperbolic tangent blending window. While effective, this method has three key disadvantages. The useful length of the parent signal is reduced, and there is no control of the spectral content of the blending region. The method also has an unfortunate tradeoff between the smoothness of transition and the useful data length. If only a small portion of the signals are overlapped and the beginning and ends of the signal are dissimilar, the transition is abrupt.

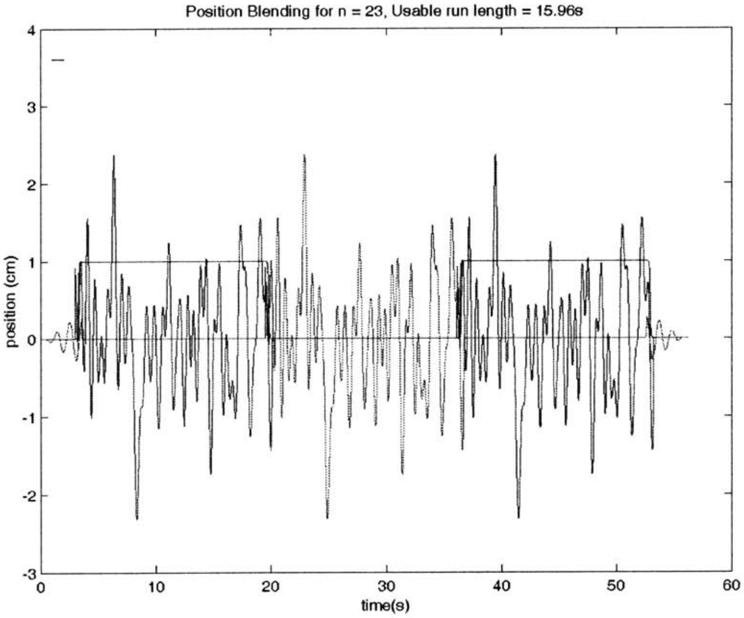

Figure 2-2: "Shift and Blend" type signal concatenation

The "shift and blend" method was eventually discarded in favor of band-limited data extension techniques borrowed from audio and image reconstruction. Two main classes of data-extension techiques were considered: non-iterative auto-regressive(AR) modelling based methods[7] and iterative Papoulis-Gerchberg type algorithims[18].

The AR modelling based approach was adopted after analysis showed it to be the most stable for a variety of gap lengths and signal phases. This method has a number of advantages over the "shift and blend" technique. Most importantly, the original signal is preserved in its entirety. Also, the blended region has a spectral content similar to the parent signal.

Per [7] the steps needed to implement the blending are as follows:

1. Estimate a high order AR model of the signal
2. Forward Extrapolate the signal across the gap by exciting the model with zero padded excitation
3. Backward Extrapolate the signal that succeeds the gap
4. Cross Fade

Each of the steps are discussed in the next section.

Model Estimation

The first step is to estimate a high order autoregressive model of the signal. An autoregressive model of a process is one where the present value of the system is the sum of P past values of X, multiplied by P filter coefficients α_p, plus zero mean white noise excitation with variance ν and some forward prediction error ε_t 2.3.

$$X_t = \nu + \alpha_1 X_{t-1} + \ldots + \alpha_p X_{t-p} + \varepsilon_t \tag{2.3}$$

If the transfer function of the system were represented as a ratio of laplace polynomials, it would contain only poles.

There are a number of detailed descriptions(Wu[27] and Roth[7]) of how the filter coefficients can be easily calculated. The approach taken (known as Burg's algorithim) is a minimization of the sum of the least squares prediction errors under a constraint on the filter coefficients. The least squares error used is the sum of the forward and backward and prediction errors. Matlab contains a number of routines for the efficient calculation of these coefficients.

Nailong Wu [27] provides us another, perhaps more insightful way of looking at the data extension technique. Rather than viewing the method as applying an autoregressive model to a process that is not generally autoregressive, Wu proves that using Burg's algorithim is equivalent to an extension by the Maximum Entropy Method(MEM) [27, pp. 69-72]. The maximum entropy method states of all possible data extensions the one using Burg's algoritim is the that has the maximum entropy. Entropy is defined by equation 2.4

$$H1 = \int_{-\frac{1}{2}}^{\frac{1}{2}} log(S(f))\, df \tag{2.4}$$

S(f) is the power spectrum and the limits of integration are from -nyquist to +nyquist.

The determination of model order is left largely to rule of thumb. Research on audio reconstruction by Roth et. al. indicates that the model order for data extension should be quite high, much higher than used for spectral analysis using Burg's method.[2]. Their results showed that if the model is not high enough a vanishing effect will occur near the center of the gap due to the minimization of the least squares error [7, pp. 4]. We tried to reproduce this effect for one of the DNS heave motions in Figure 2-3. Instead of the vanishing effect observed by Roth [7], the data extension behaves erratically for lower model orders. Roth recommends model orders of around 1000 to avoid problems. Figure 2-3 shows that for a model order of 1000, the data extension is reasonable.

Forward Extrapolation

The AR modelling blending method is easily implement using Matlab. The procedure consists of calculating the filter coefficients, initializing the filter with P past values and feeding a vector of length W to the filter.

```
a = arburg(y,P);
Z = filtic(1,a,y(end-(0:(P-1))));
ye = filter(1,a,zeros(1,W)),Z);
```

---

[2] high order models are not typically used for MEM spectral analysis due to problems with line splitting and peak shifting

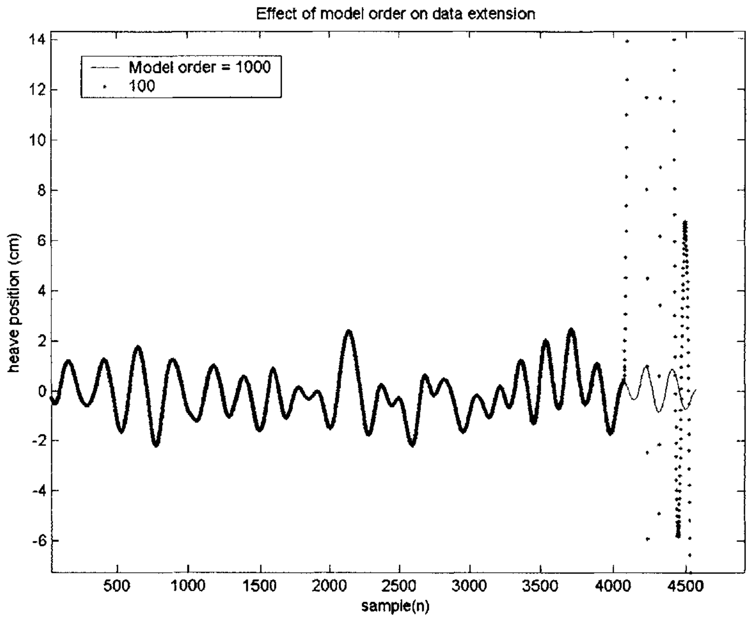

Figure 2-3: Effect of model order on data-extension

where P is the model order, y is the position and W is the length of the extension.

Backward Extrapolation The Burg algorithim is ideally suited for backward extrapolation since the least squared error is minimized with respect to the backwards error in addition to the forward error. To perform backwards extrapolation the signal is simply flipped and passed through the filter. Figure 2-4 shows the of the forward and backward extrapolation for a typical signal.

Cross-Fading The backward and forward extrapolation are then cross-faded into each other as shown in Figure 2-5. The gap length is chosen by the slopes at the beginning and end of the signal and the mean frequency, such that the fit does not produce an abrupt transition. The window used for the blending window is defined by 2.5.

$$w(n) = \begin{cases} 1 - \frac{1}{2}(2u(n))^{\alpha}, & \text{if } u(n) \leq \frac{1}{2} \\ \frac{1}{2}(2u(n))^{\alpha}, & \text{if } u(n) > \frac{1}{2} \end{cases} \tag{2.5}$$

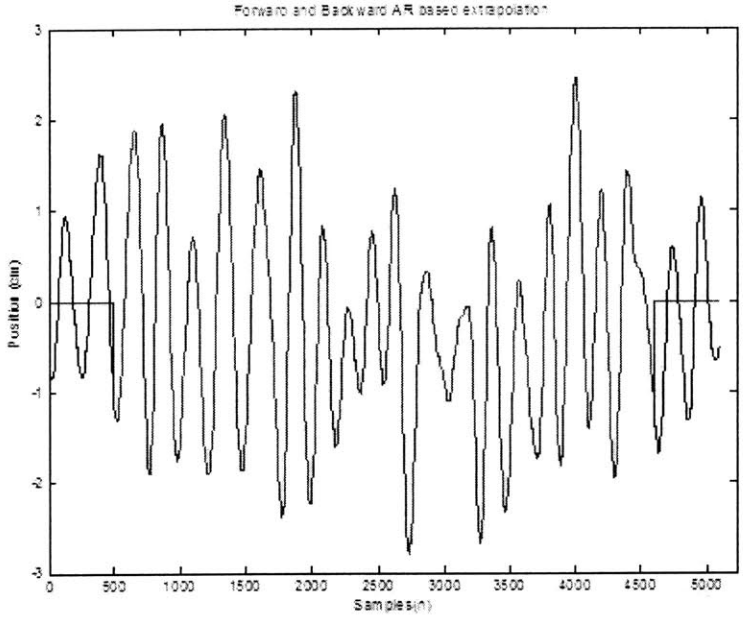

Figure 2-4: Backward and Forward Data Extension via AR Method

where $u(n) = (n - n_s)/(n_e - n_s)$, n(s) is the starting sample, n(e) is the ending sample, and n is the current sample. The parameter α can be varied to increase the steepness of the window. Following the work of Roth [7], an α of 3 was used for all blendings.

An interesting way of looking at the the effect of the blending on the response would be to remove part of a known signal and replace it with the blended signal[3]. Obviously, the the phases and amplitudes of the blended section are going to be different than the actual signal, but the spectra of the lift signal should be similar. This raises the question, if the blended region are short in length compared to the overall run, is one justified in including them as part of the signal in the spectral analysis? Doing so could significantly improve the spectral resolution and/or confidence intervals of the spectral estimates.

Once the signal has been properly concatenated, the position signal is resampled to the desired control rate using an FFT based method, differentiated, and written

---

[3] This is going to be tried in the next round of testing

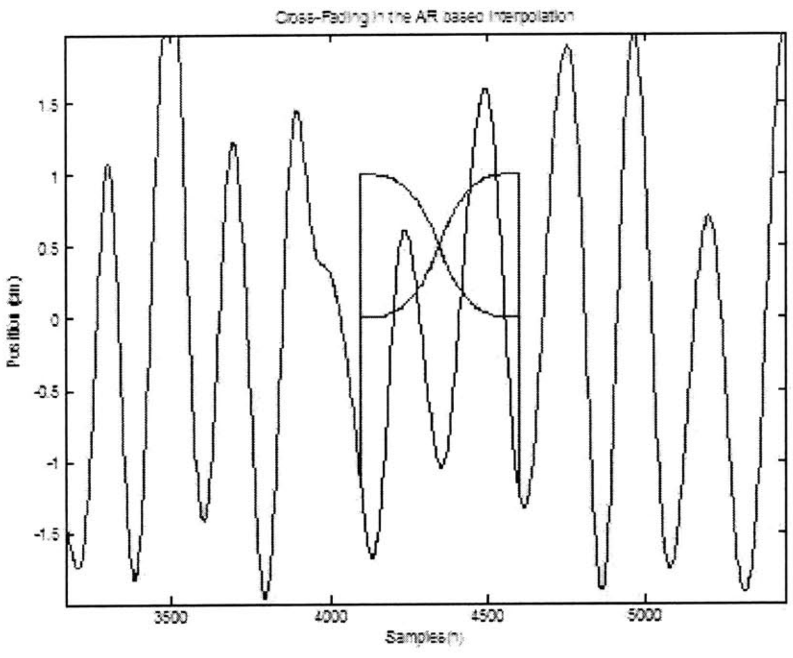

Figure 2-5: Cross-Fading of Signals

to an ASCII file to be read by the control code.

2.3 Control Code and System Validation

The control code used for the experiments is a modification of the code developed by Smogeli [22] in 2002. To tailor the code for the needs of these particular experiments, the capability to read a file of commanded velocities to a buffer was added. Like previous VCTA experiments, velocity control was chosen chosen over position or torque control in order to improve the smoothness of motion.

Velocity control does have a number of idiosyncracies that had to be addressed. The integration of the velocity errors tends to cause the position to drift slightly over the course of the run. For a typical run, this drift amounts to around 5% of a diameter over 4 concatenated signals. The effect of this slowly varying drift on the hydrodynamics however should be minimal as it is the velocity and accelation that influence the fluid forces. The position would only come into play if there were shallow water or free surface effects taking place. To ensure that all the tests being carried out at roughly the same starting depth, the test cylinder is recentered regularly.

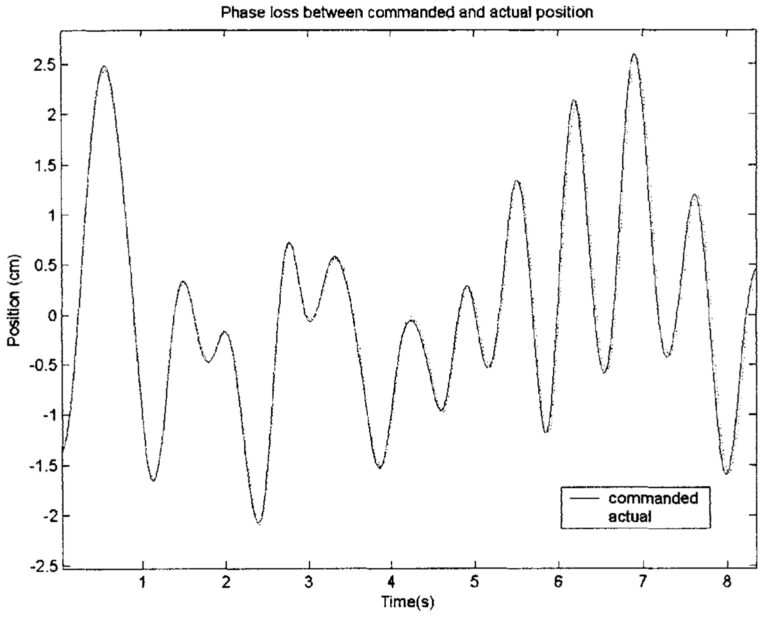

Figure 2-6: Typical Phase Loss between commanded and actual position

As seen in Figure 2-6, phase loss occurs when the VCTA is run in tracking mode. This phase loss is typically around a degree or two over the course of a run. The phase loss is consistent with what was reported by Miller [15, pp.34] for similar frequency forced vibrations. While this seems pretty minor, it could heavily influence C_{LV} if the commanded motion were used instead of the actual measured motion in the calculation. For this reason the measured motion is always used in lift phase calculations. Using the MEI motion exerciser, the motor is tuned with quite a bit of velocity feed forward to try and minimize phase loss.

The overall tracking performance for a typical run can be summarized, σ is the standard deviation of the signal

Coherence at top 3 Dominant Frequencies	99%
Mean position error as percent of signal σ	$< 1.5\%$
Position repeatability as percent of σ	$< .5\%$
Phase Loss over signal length	$\approx 1 - 2$ deg

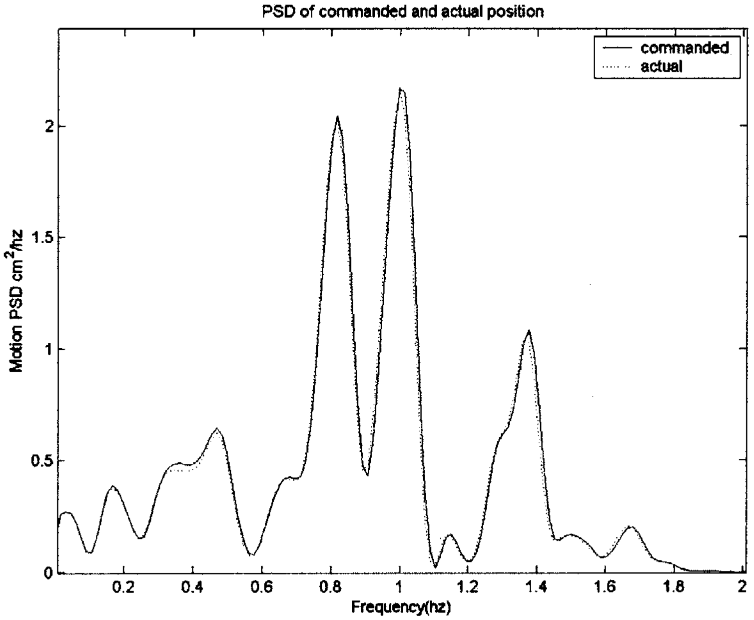

Figure 2-7: Typical Commanded and Actual Position Spectra

Figure 2-7 is a comparison of the commanded and actual motion spectra as measured by the LVDT. There is good coherence at the dominant and subdominant frequencies.

The position of the cylinder is measured both by the LVDT and a vane encoder attached directly to the tailshaft of the servo motor. Both these devices give complimentary position measurements. Using the gain for the LVDT colibration and the motion exerciser, it was determined that conversion from meters to encoder counts is 159345 counts/meter, this factor is within 1/10 of a percent of the value used in the Smogeli's control code header files [22, pp. 10].

The lift and drag forces are measured at the support points of the cylinder using 3-component piezoelectric force sensors. These sensors emit a charge signal proportional to the shear force on the sensor. The signal is sent to the charge amplifier where it is converted a voltage to be used either in a feedback loop or acquired. The sensors are calibrated with the cylinder in place so that the reaction forces do not need be considered. The calibration procedure consists of adding and removing known weights by means of a pulley system. Figure 2-8 contains an example calibration curve. They are typically very linear with R^2 values from .99 to .999. Calibration is repeated before and after each set of tests. Learning from Smogeli's experiments [22] steps are taken to properly preload the force element, prevent cable flexure, and minimize amplifier drift.

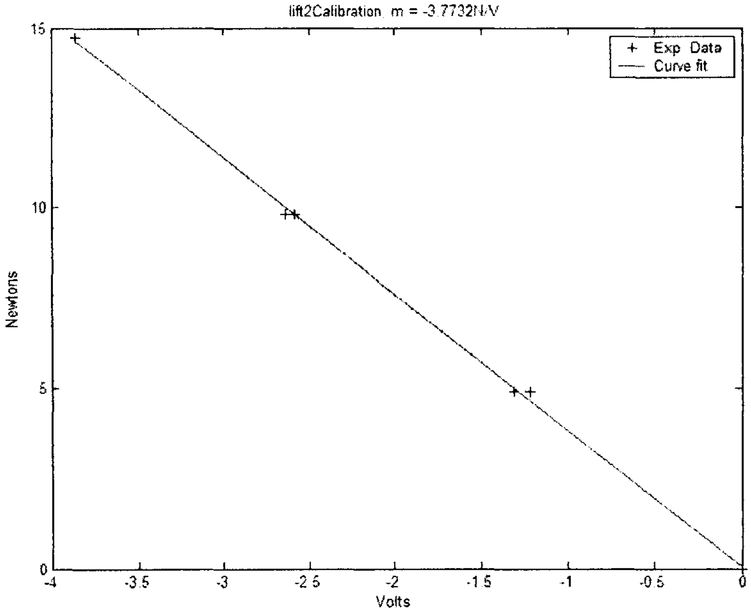

Figure 2-8: Typical Force Sensor Calibration

Chapter 3

Experimental Data Analysis

3.1 Properties of the Commanded motions

When developing tools to analyze the force data and cylinder motions from the experiments, two principal types of questions have to be addressed: Type 1) What is the internal structure of the data? Type 2) What is the joint structure, or dependence between data sets?

Recalling Figure 1-9, we see that the heave motions to be imposed on the VCTA are intricate, often comprised of many frequencies evolving in time. A natural way of handling Type 1 questions on irregular time series such as Figure 1-9 is to decompose the data set into its periodic components through Fourier analysis. In the frequency domain, one can tell which frequencies contribute prominently to the overall signal power. Fourier analysis, however has to be applied carefully since these time series are only weakly stationary. The motions of freely vibrating bodies such as the flexible cylinder in the simulation are never truly constant in amplitude and frequency.[20, pp. 395]. To determine the extent of the modulations, tools from Time/Frequency analysis such as the Short-Time Fourier Transform (STFT),Complex Demodulation [2, pp. 97-132] and Empirical Mode Decomposition(EMD)[10] were explored and adopted. These methods are discussed in the following sections.

3.1.1 The importance of lift force phase

One of the key Type 2 questions in VIV research is the interdependence of the fluid forcing and cylinder motion. A revealing quantity in looking at this relationship is the phase between the the lift force and the cylinder motion. Positive ϕ_0 (force leading motion), indicates that power (related to the sine of ϕ_0) is flowing from the fluid to the body, which in turn responds by moving with a lag. The phase is a good indicator of the vortex patterns near lock-in, where very small changes in motion frequency can produce very large changes in phase. Lift force phase has also been shown to be an important quantity when comparing the results of forced and free vibration experiments [20, pp.395].

3.1.2 C_{LV}, C_{LA} and C_{Mo}

The phase angle is used in the typical decomposition of the lift force into an inertial component in phase with the acceleration of the motion and a viscous/ negative damping component in phase with the velocity of the motion. The form of lift force is given in Equation 3.1 for a single mono-component input motion at f_{ex}:

$$C_L(t) = (-C_{Lo}cos(\phi_0))sin(2\pi f_{ex}t) + (C_{Lo}sin(\phi_0))cos(2\pi f_{ex}t) \tag{3.1}$$

where C_{Lo} is the total measured lift coefficient, and ϕ_0 is the phase angle. The term $(-C_{Lo}cos(\phi_0))$ is aptly called the "lift in phase with acceleration" or C_{La}. It is related to the added mass by Equation 3.2. The term in phase with the velocity, $(-C_{Lo}sin(\phi_0))$ is represented by the symbol C_{Lv}. These coefficients are very non-linear functions of motion amplitude and frequency.

$$C_{Mo} = \frac{-U_{exp}^2 C_{La}}{2\pi^3 A Y_0 f_{ex}^2} \tag{3.2}$$

The added mass is a non-linear function of frequency and amplitude and only approaches its potential flow value when the frequencies of oscillation that are much higher than the shedding frequency.

Since the input motion is composed of many frequencies of various amplitudes, it is guaranteed that these coefficients will assume different values for each frequency. If amplitude and frequency modulation occurs, the coefficients will change in time as well. To deal with both these cases an efficient formulation of C_{Lv}, C_{La}, and C_{Mo} for each component frequency was developed and is presented in the following section. Derived in Section 3.4 are equivalent expressions for use with complex demodulation.

It is also of interest to be able to quantify the degree of similarity between the DNS and the experimental force measurements. This is accomplished in the time domain by means of moving windows and in the frequency domain by the coherence function. Similar methods are used to look at the repeatability of runs and end force correlation.

3.2 C_{LV},C_{LA} and C_{Mo} as a function of frequency

The natural first step in extending the single component equations for C_{LV} and C_{LA} (Equation 3.1) to ones where the force and motions are sums of sinusoids is to find an expression for the relative phase between the time series.

Recognizing that the Fourier transforms of the motion and lift coefficient, $X(f)$ and $C_L(f)$ can be written in polar form, $|X(f)|e^{2\pi i\Phi_x(f)}$ and $|C_L(f)|e^{2\pi i\Phi_{C_L}(f)}$, the relative phase can be found by multiplying $C_L(f)$ by the complex conjugate of $X(f)$, that is

$$I_{C_L,X} = C_L(f)\overline{X(f)} = |C_L(f)||X(f)|e^{2\pi i(\Phi_{C_L}(f)-\Phi_x(f))} \tag{3.3}$$

The lift force angle is given by $\Phi_{C_L,X} = tan^{-1}(\frac{\Im I_{C_L,X}}{\Re I_{C_L,X}})$

In many cases the C_{LA} and C_{LV} values as a function of frequency are of primary interest. Returning to Equation 3.1, C_{LV} can be written as

$$C_{LV}(f) = |C_L|sin(\Phi_{CL,X}) = \frac{\Im C_L(f)\overline{X(f)}}{|X(f)|} \tag{3.4}$$

The last form of C_{LV} is arrived at by solving 3.3 for the second term in 3.4.

As a practical matter, the fast fourier transform is normally used to compute these coefficients. To properly scale $C_{LV}(f)$, Equation 3.4 needs to be divided by the length of the fast fourier transform (FFT), N. Equation 3.5 is in the FFT ready form.

Another practical matter involves the use smoothed estimates of $I_{C_L,X}$ and $|X(f)|$. Smoothed estimates are made by finding the $I_{C_L,X}$ and $|X(f)|$ of segments of a signal and bin averaging. This process while seemingly beneficial tends to under predict the $C_{LV}(f)$ due to the fact that the magnitude of the smoothed estimate $|\hat{I}_{C_L,X}|$ is $\leq |X(\hat{f})||\hat{C}_L(f)$ (inequality shown in Bloomfield [2, pp.206]). Because of this, the C_{LV} are calculated for each segment and then averaged.

FFT ready forms of the equations for $C_{LV}(f)$,$C_{LA}(f)$ and $C_{Mo}(f)$ are shown below.

$$C_{LV}(f) = |C_L| sin(\Phi_{CL,X}) = \frac{2\Im C_L(f)\overline{X(f)}}{N|X(f)|} \tag{3.5}$$

$$C_{LA}(f) = -|C_L| cos(\Phi_{CL,X}) = \frac{-2\Re C_L(f)\overline{X(f)}}{N|X(f)|} \tag{3.6}$$

$$C_m(f) = \frac{-U_{exp}^2 C_{LA}(f) N}{4\pi^3 (f)^2 |X(f)| D_{exp}} \tag{3.7}$$

3.3 Fourier Analysis

As seen in the previous section, Fourier analysis is a valuable tool for our analysis, allowing the computation of $\Phi_{CL,X}$ simply from the cross-spectrum of the motion and lift coefficient (Equation 3.3). Fourier analysis is also useful for quantifying the correlation between the DNS and experiment at each frequency and in visualizing the frequency and amplitude modulations of the signal. To estimate the modulations, spectral analysis is applied to small segments of the signal. These Short-Time Fourier Transforms (STFT) are calculated at a number of time steps and then plotted to create what is known as a spectrogram.

The preliminary steps for carrying out each of these tasks are nearly identical.

The goal of these first steps is to create auto and cross periodiograms, or single observations of the spectra to be estimated, for segments of the time series. The segment lengths and data windows are chosen to achieve the required frequency and time resolution.

To summarize, the steps taken are

1. Low-Pass Filter if necessary
2. Remove mass-inertial component of lift force
3. Separate the time series into segments
4. Detrend the time series
5. Window the series using a cosine taper
6. Zero Pad for spectral interpolation
7. compute periodogram

Time Series Segmentation: The frequency resolution of a spectral estimate, or the ability to discern between two nearby peaks, is determined by a number of factors. The two main factors that influence the resolution, f_w, are the length of the time series, N and the sampling rate, f_s, $f_w = f_s/N$ is the upper bound of the resolution. Because the sampling rate is set by the experimental set-up (typically 250hz) or by the time resolution of the DNS, the frequency resolution is tuned with the data length. Other operations such as windowing and bin averaging tend to reduce frequency resolution. In cases like the power spectrum of the lift or motion, where the regularity between segments of the signal is of interest, the segment length is typically set fairly large, so as to get the non-dimensional frequency resolution below .015. Examination of a number spectra obtained by using the maximum available data length has shown that this is sufficient to resolve almost all of the dominant frequencies in the DNS. In order to obtain the best estimate of the underlying spectrum, the run length isn't increased to its maximum. Increasing data length will no have no effect on the confidence intervals for the spectra, because a long record only provides a single observed value of the spectra. It is for this reason that repeat runs are also performed. This can be clearly seen in Figure 3-1. As expected, the confidence in the power spectrum estimate increases with the number of runs/number of segments. In order to maximize the number of segments, they are chosen such that they overlap(Welch's method). For details on how the approximate confidence intervals shown in Figure 3-1 are calculated and the assumptions involved, please see Bloomfield [2].

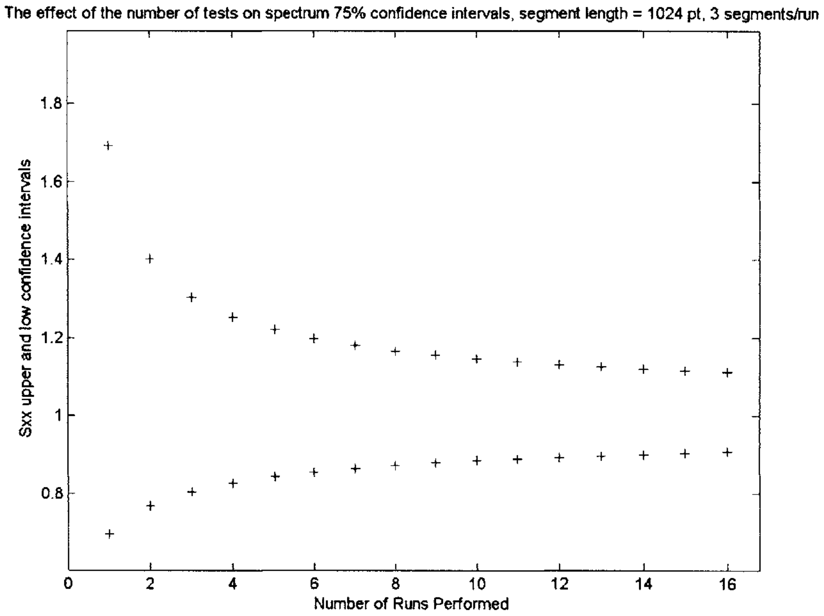

Figure 3-1: Effect of Number of Runs on 75% Confidence Intervals

The factors governing the segment length choices for the spectrogram are somewhat different from those influencing spectrum estimates. In the spectrogram the aim is to be able to show the evolution of the frequency and amplitude with time. This requires the data segments be chosen short enough to show the changes in time, and long enough to resolve the frequencies of interest. A good to think of this trade off between time and frequency resolution is to think of a dirac function. A dirac function in the time domain is perfectly localized, yet in the frequency domain spans all frequencies. Conversely, a dirac in the frequency domain spans all time. With the spectrogram $= |STFT|.^2$ [1], localization in time *and* frequency is not possible and a compromise has to be made. However, with proper segment length choice, it can yield results similar to the methods such Wigner-Ville transform and wavelets without some of their drawbacks. Experiments showed that a segment length of 2 cycles was sufficient to capture the general behavior of the signal. This segment length corresponds to a non-dimensional frequency resolution of around .04 or better. Because of the close proximity of dominant frequencies in VIV, this but enough to resolve everything of interest, but is good enough to notice trends in the mean frequency. The variation of the mean frequency displayed in the the Results section and the Appendices was calculated using this method.

Effect of Windowing A signal of finite duration can be viewed as the multiplication of an infinite time series by a rectangular window. In the frequency domain this corresponds to a convolution of the fourier transform of the boxcar (a sinc) with the true spectrum. This convolution produces spurious sidelobes that can be misinterpreted. One of the most common ways of reducing these sidelobes is to multiply the signal by something more periodic than the boxcar. Data windows that are variations on a cosine bell are often used.

The windowing process also introduces less desirable effects. As can be seen in the curve for the Hanning window in Figure 3-3, the peaks of the power spectrum for the windowed time series are broader than for the nonwindowed spectrum and the amplitude has been reduced. It can also be shown that the variance of the estimate increases when windows are used [2]. This increase shown in Figure 3-2 is fairly minor though, as the confidence intervals are more heavily influenced by the number of segments. Due to the need to preserve high frequency resolution, a 20% cosine taper was chosen. The 20 % refers to

---

[1] this is simply the power spectrum, a STFT is the Fourier transform of the signal after it has been windowed to leave only the segment of interest

the total percentage of the segment that is tapered. On a 20 % cosine taper window, the first and last 10 % is tapered. The peak of the untapered spectrum in Figure 3-3 is matched almost perfectly by the one using the 20 % taper, we can also see that some of the side lobes in the low frequency range are reduced.

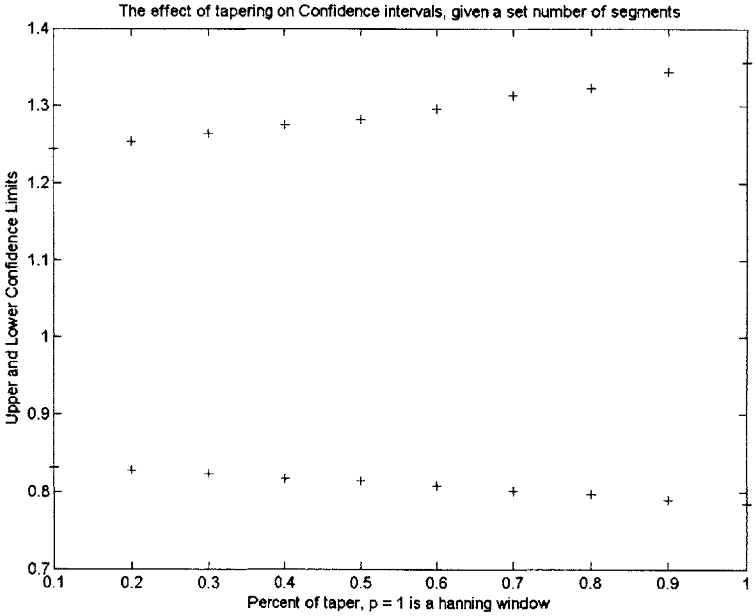

Figure 3-2: Effect of Cosine Taper on 75 % Confidence Intervals

Once the time series have been segmented, detrended and windowed, the periodograms are calculated. This calculation is usually carried out with the FFT, making sure to properly normalize by the power of the of the data window.

If C_{LV} or C_{Mo} are to be calculated Equations 3.7,3.7,3.7 are used. As described earlier, the values are first calculated and then averaged.

If power spectral density estimates are to be made, the periodograms are bin averaged, made one sided and scaled by the sampling frequency. The amplitudes of motion at the dominant frequencies are often recorded.

In the case of the periodograms used for the spectrogram, they are left alone and plotted vs. time. To find the approximate variance in frequency, the mean frequencies at each time step are found from the spectral moments.

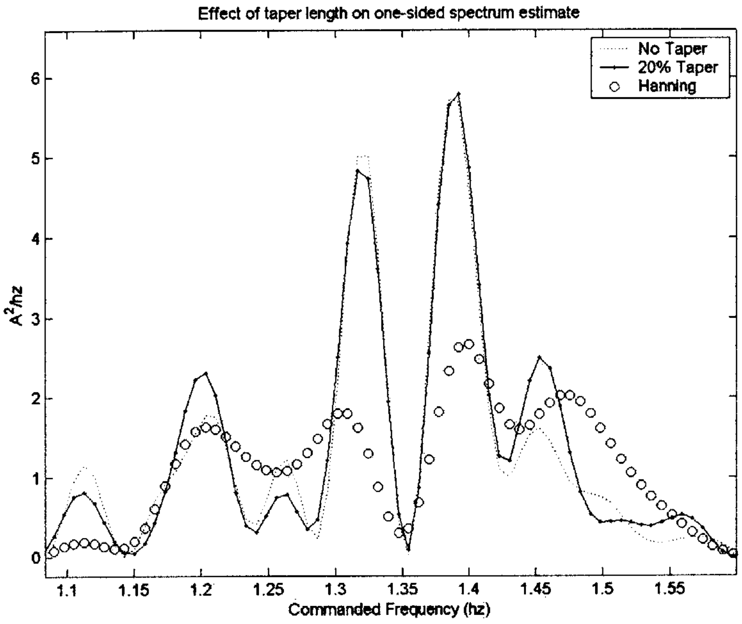

Figure 3-3: Frequency Resolution loss with windowing

3.4 Complex Demodulation

An alternate, equally valid approach to analyzing the force and motion data is to view the signals as being composed of sinusoids of form 3.8. Unlike in Fourier analysis, where the amplitude and phase of a given harmonic are constant, the amplitude and phase in 3.8 are allowed to change slowly over time. This type of decomposition is well-suited for the non-linear, history dependent nature of free vibrations [20]. As was shown by Krishnamoorthy [12], even at the critical lock-in frequency, where the wake structure transitions from 2S to 2P, the lift force phase oscillates and doesn't change abruptly. Much can be learned from this approach, even when it fails. Qualitative knowledge that the phase isn't slowly varying, may may indicate a change in frequency, or other phenomena. This type of an analysis can help describe features of the response that may be missed by harmonic analysis, and can be used to better interpret the results from harmonic analysis.

The goal of *complex demodulation*[2] is to extract approximations for $R(t)$ and $\phi(t)$. This is accomplished by forming the series 3.9 by multiplying $x(t)$ by a complex sinusoid of frequency f0, the frequency of interest. This demodulation acts to zero the frequency scale to f0. As can be seen in Equation 3.9 this creates a term from which R(t) and $\phi(t)$ can be extracted. The process also introduces a complex sinusoid of frequency -2f0 with varying phase. R(t)is simply the twice the modulus of the first term, and $\phi(t)$ is the argument(Equation 3.10). The second term has to be filtered out.

The main problem in complex demodulation is then one of filtering. In the case of a sum of sinusoids with varying phase and amplitude in the presence of noise, the filter has to carefully designed such that it rejects noise and sinusoids of other frequencies(all shifted by -f0 in the demodulation). The filter used in the analysis is a 5th order low pass Butterworth filter with a cutoff frequency set at half the frequency separation between dominant frequencies. The filter is implemented using the acausal function filtfilt in Matlab to ensure zero phase. The use of filtfilt is equivalent to two passes of the filter and doubles the order.

One of the most revealing applications of complex demodulation is in estimating the time varying relative phase between force and motion. To do this, one demodulates both the force and motion signal at the same frequency and computes the difference of $\phi_{CL}(t)$ and $\phi_Y(t)$. Care must be tken to properly unwrap the phase. Once the relative phase is computed, Equations 3.1 and 3.2 can be applied to find the lift in phase with velocity and added mass using the slowly varying lift amplitude. The frequencies on which to demodulate are usually chosen from the peaks of the input motion power spectrum. In these experiments the top four dominant frequencies are analyzed. Figure 3-4 is the complex demodulation of a mono-component fixed vibration experiment. As expected the magnitude of the motion is constant, being a pure sinusoid, while the $|C_L|$ and C_{LV} from the relative phase, varies over the course of the run. Another comparison possible with complex demodulation is the relation between the time varying amplitudes of the lift and motion. In strip theory these should be close to linearly related for constant f, as the velocity and acceleration are functions of R(t). However, as will be seen in the next section, this is often not the case for the simulation.

Complex demodulation is closely related to the power spectrum. In a sense it is a type of local harmonic analysis that sacrifices some frequency resolution for time resolution. The relation between the value of R(t)(f0) and a power spectrum at the same frequency is given in Equation 3.13. It can be shown [2] that this power spectrum is of the same type as one produced by bin averaging. The variables α_u in the denominator are the coefficients of the low pass filter.

$$x(t) = R(t)cos(2\pi(f_0(t) + \phi(t))) = 0.5R(t)(e^{2\pi i(f_0 t+\phi(t))} + e^{-2\pi i(f_0 t+\phi(t))}) \tag{3.8}$$

$$y(t) = x(t)e^{-2\pi i(f_0 t)} = 0.5R(t)e^{2\pi i\phi(t)} + 0.5e^{-2\pi i(2f_0 t+\phi(t))} \tag{3.9}$$

$$z(t) = 0.5R(t)e^{2\pi i\phi(t)} = u(t) + iv(t) \tag{3.10}$$

$$R(t) = 2\sqrt{u(t)^2 + v(t)^2} \tag{3.11}$$

$$\phi(t) = tan^{-1}(v(t)/u(t)) \tag{3.12}$$

$$S_{xx}(f0) = \frac{\sum R_t(f0)^2}{N\sum \alpha_u^2} \tag{3.13}$$

3.5 The Hilbert Transform and related methods

Very often when the time series are demodulated, a linear trend in the time varying phase is present. Following Equation 3.8 this trend can be interpreted as a shift in frequency. It also indicates that the frequency chosen for demodulation is not dominant for the whole stretch of data, even though it may represent a peak in the power spectrum. To better understand these frequency changes, time frequency

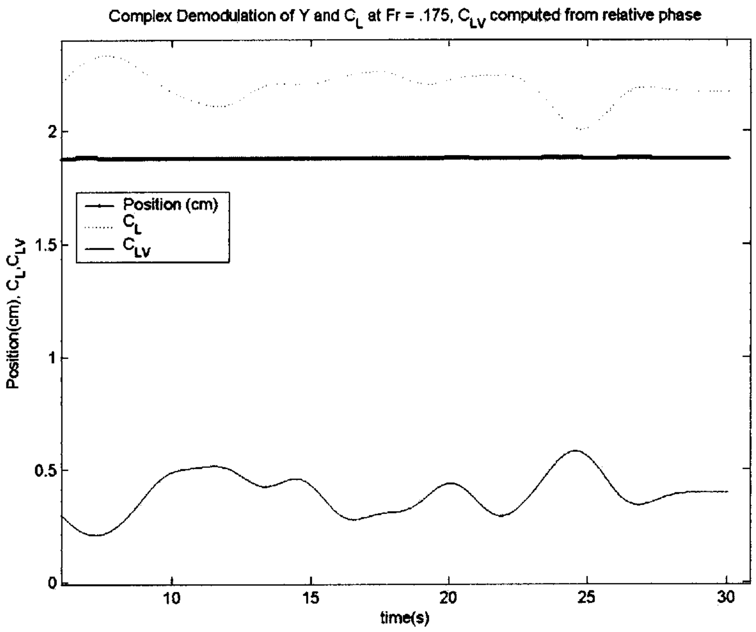

Figure 3-4: $|C_L|$, $|Y|$, and C_{LV} from Complex Demodulation Analysis of a Purely Sinusoidal Input Motion

tools such as the spectrogram were investigated. However, as mentioned before, the spectrogram is not without it's limitations. To try overcome some of these limitations, another relatively new class methods based on the Hilbert Transform was explored. These tools can provide a very rough estimate of the instantaneous frequencies (IF) for a multi-component signal. These too have their own severe limitations, but it is hoped that in conjunction with other methods discussed, we may shed light on the frequency variations in the data.

The instantaneous frequency for a mono-component signal is most often found from the Hilbert transform. Recalling Equation 3.8, we observe that a real signal such as a sum of sinusoids consists of both positive and negative frequencies, and that the information contained in the negative frequencies is redundant. The Hilbert transform is used to construct a version of the signal that contains only positive frequencies, and maintains the signal power. One of the main advantages of doing this is that the average frequency of the signal becomes positive.

Equation 3.15 shows the method in which the analytic signal, z(t) is created from x(t). To ensure that z(t) contains only positive frequencies, the imaginary part of this signal has to be the Hilbert transform of x(t), given in Equation 3.14. Calculation of the Hilbert transform is straightforward and can be carried out by the function Hilbert.m in Matlab.[2]. It consists of taking the Fourier transform of x(t), multiplying the transform X(f) by -i for negative frequencies, +i for positive frequencies, and taking the inverse transform. For more information on the Hilbert Transform, see *Time Frequency Signal Analysis* by Boualem Boashash [3].

$$H(x(t)) = F^{-1}_{t \Leftarrow f}\{(-isgn(f))F_{t \Rightarrow f}(x(t)\} \tag{3.14}$$

$$z(t) = x(t) + iH(x(t)) = a(t)e^{i\phi(t)} \tag{3.15}$$

$$f_i(t) = \frac{1}{2\pi}\dot{\phi}(t) \tag{3.16}$$

To find the instantaneous frequency of the signal from the analytic signal, we write z(t) in polar form and take the derivative of the the argument. For narrow band signals, the IF from the Hilbert transform may be interpreted as a mean frequency. It can be shown [3, pp. 25] however, that for wider band signals or ones where the envelope gets small, the instantaneous frequency can give erratic results such as infinite or negative frequencies. Figure 3-5 shows the instantaneous frequency for one the input motions. Smoothing of the signal may reduce the variability a little, but in general the method of finding the IF from the Hilbert transform is not directly applicable to the results from these experiments.

If, however we could decompose our signal into a sum of narrow band functions with near constant envelopes, the Hilbert transform could give meaningful results. One novel method of performing such a task is known as empirical mode decomposition (EMD), proposed by Huang in 1998[10]. The method seeks to break a non-

---

[2] the function Hilbert.m in Matlab returns the complete analytic signal, not just the Hilbert transform

stationary signal into what are known as intrinsic mode functions (IMF) using an iterative process. The result of this process are functions that generally satisfy the necessary conditions for finding the instantaneous frequency via the Hilbert transform. The conditions on the IMF's includes properties such as no inflection points between extrema and zero mean[3]. Due to the algorithmic/data-driven nature of the solution, EMD sometimes produces modes that are not truly IMF's. Additionally, performance quantities such as confidence intervals are difficult to estimate. Most importantly, it must be stressed that these intrinsic modes *are not* physical modes of the system the and are only loosely orthogonal. Even, so this technique has been successfully applied to problems in a number of fields, particularly in nonlinear wave mechanics and metereeology.

Once the IMF's are found, the instantaneous frequency and amplitude can be computed for each mode by forming analytic associates of the modes. These can be presented in a distribution of frequency and amplitude vs. time known as the Hilbert Spectrum. It has been shown that the decomposition can yield similar results to wavelets but with potentially better time/frequency resolution.

The algorithm used for EMD is described below. In the literature, the process is known as sifting for mode functions.

1. Determine the mean of the upper and lower envelopes of the signal, $m_1(t)$. This is usually done by a cubic spline interpolation of local maxima and minima.
2. Remove $m_1(t)$ from the data, forming h_1, $h_1(t) = x(t) - m_1(t)$
3. Repeats steps 1 and 2, using $h_1(t)$ as $x(t)$ until convergence $h_{1,(k-1)}(t) - m_{1,k} = h_{1,k}$
4. Set aside $h_{1,k}$, this is the first IMF
5. Subtract $h_{1,k}$ from $x(t)$ and repeat steps 1-5, to find$h_{1..n,k}$
6. Stop when the result of the process produces something with a nonzero mean, or inflection points between extrema.

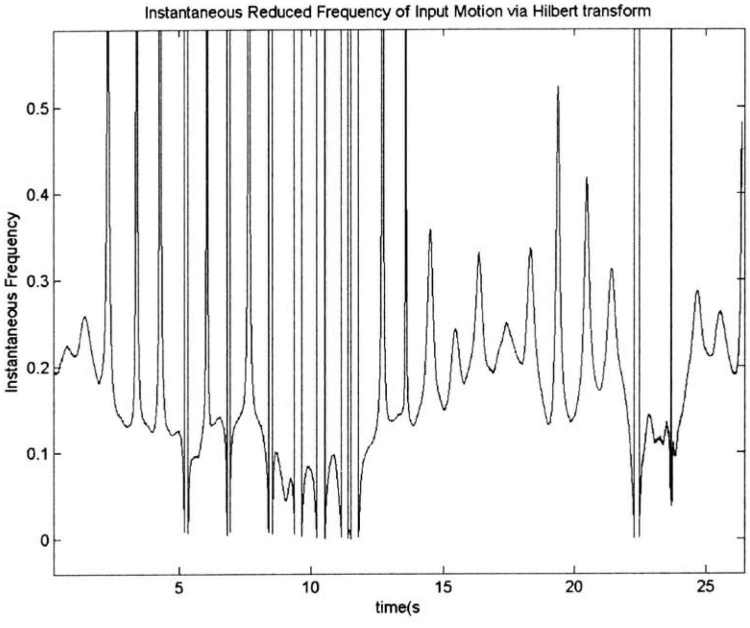

Figure 3-5: Instantantaneous Reduced Frequency of Input Motion via Hilbert Transform

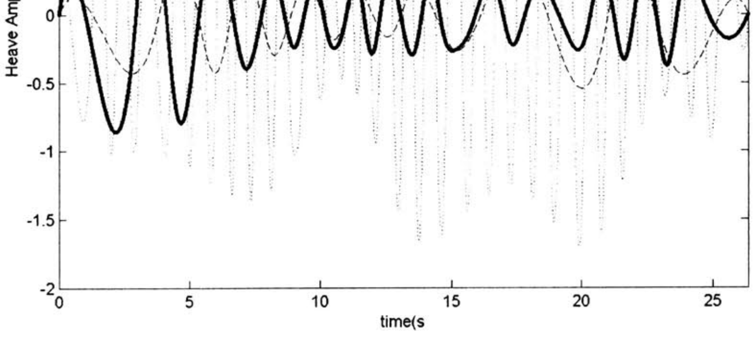

Figure 3-6: First 3 IMFs of a typical input motion

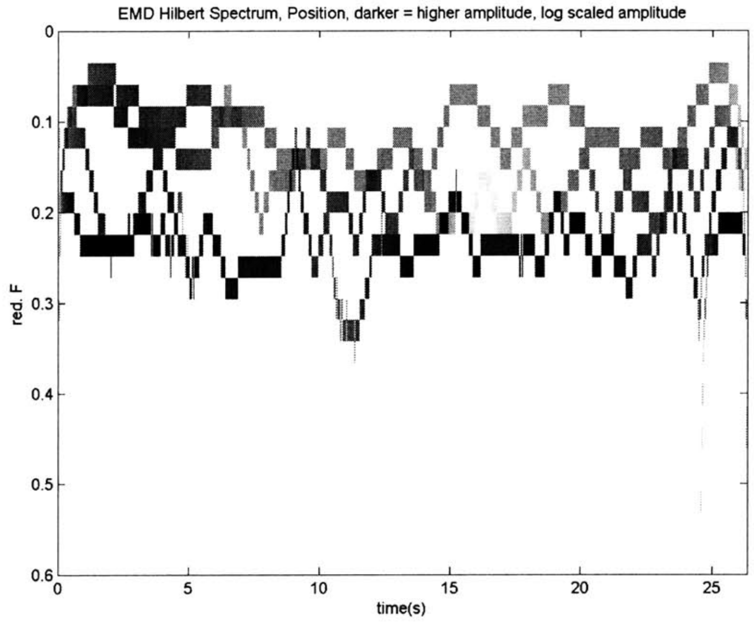

Figure 3-7: EMD Hilbert Spectrum of Input Motion, Darker = higher amplitude

Shown in Figure 3-6 are the IMF's of an input motion signal. The input motion signals typically can be broken down into less than 10 IMFs, of these only three or four contain significant energy. Figure 3-7 contains the Hilbert spectrum created from these IMFs. The ridges provide a rough estimate of the average frequency, and amplitude as a function of time. Again, the "modes" themselves have little or no physical meaning.

3.6 Time Domain analysis

In addition to the frequency and time/frequency methods discussed above, a number of statistics are computed directly from the time series from each run. These can be useful in quantifying the correlation between DNS and experiment, identifying key events and validating experimental methods.

The workhorse of the time domain analysis is the correlation coefficient, defined

---

[3] Interestingly, there is an ever growing number of constraints on the definition of an IMF

in Equation 3.17. In an inequality related to the one mentioned in Section 3.2, the magnitude of the covariance of two signals must be less than product of the individual signal magnitudes. The correlation coefficient provides a number between -1 and 1 that gives us information about the phase between signals. The $x(t)^2$ term in the denominator is the inner product of x(t) with itself, or the autocorrelation at zero lag. To compare the magnitudes of two signals, different statistics such as RMS values and the coherence are computed.

Gopalkrishnan[9] and others have used an equation similar to that the correlation coefficient for calculating C_{LV} and C_{LV}. The "Inner Product" forms of C_{LV} and C_{LA} are given in Equation 3.18. These are calculated for each run and provide a kind of global value for these coefficients. For pure sinusoidal cases, this result of 3.18 is equivalent to that in equation 3.1. For a beating oscillation, 3.18 may be interpreted as the coefficients that "when applied to a sinusoidal waveform at a carrier frequency f_c and of the same RMS amplitude, yield the same RMS output power". We also try and approximate the global C_{LV} and C_{LA} as a function of time using moving windows of approximately two cycles in length. These provide a good check for the values from complex demodulation.

$$C_{xy} = \frac{\langle x(t), y(t)\rangle}{\sqrt{\langle x(t)^2, y(t)^2\rangle}} \tag{3.17}$$

$$C_{LVip} = 2\frac{\langle C_L(t), \dot{y}(t)\rangle}{\sqrt{\langle 2\dot{y}(t), \dot{y}(t)\rangle}} \tag{3.18}$$

$$C_{LAip} = 2\frac{\langle C_L(t), \ddot{y}(t)\rangle}{\sqrt{\langle 2\ddot{y}(t), \ddot{y}(t)\rangle}} \tag{3.19}$$

The correlation statistic is also used to look at end force correlation. In previous work this statistic has been shown to be a good indicator of three dimensionality and lock-in (see [5]). To look at the correlation between the DNS and the experiment, a process similar to the one used to construct a spectrogram is used. We compute the correlation in a moving window of approximately two cycles in length. Other statistics such length of time that the correlation is above a certain limit are also calculated. In most case signals with correlation above .5 are considered correlated.

Chapter 4

Results of Experiments

To validate the experimental set-up, tests were first carried out using monocomponent input motions. Tests such as these have been studied extensively by researchers at MIT and elsewhere[9],[25],[20]. The results of these experiments compared favorably with past results and motivated further research. The sinusoidal motions were also a proving ground for the post processing techniques described in the previous chapter

The second set of tests consisted of imposing the motions observed on a flexible cylinder in uniform inflow. This set of experiments was vital in establishing a basis of comparison for the gross lift force magnitudes of the DNS and Experiment, as the uniform inflow case did not require the time/frequency scaling described in Chapter 2.

Finally, tests were performed at various locations along the span of a cylinder in sheared conditions. Complex demodulation analysis showed that locally, the results from these experiments were very similar to 2-d studies done on beating cylinders by Gopalkrishnan and others [9],[16],[21].

Having a grasp on the response of a cylinder to 2-d beating and random oscillations, we could then begin to gage to what extent the actual 3-d behavior (DNS) was captured in the 2-d experiments. This chapter will present some representative results from the shear flow cases and discuss implications for future modeling

4.1 Base Cases

4.1.1 Previous multi-frequency studies

Beginning with Bishop and Hassan[25], there has been extensive work on cylinders forced at fixed frequency. Researchers such as Sarpkaya [20], Williamson and Roshko [25] and Gopalkrishnan[9] have mapped the cylinder forces and characteristic vortex patterns for a wide range of motions.

Motivated by the presence of beating patterns in marine cables, this work has been extended to include multi-frequency tests. Systematic tests by Schargel [21], Nakano and Rockwell [16], Gopalkrishnan have distilled many of the key attributes of the cylinder response to multi-frequency forced vibrations.

Schargel in his Master's thesis entitled "Drag Forces on a Randomly Vibrating Cylinder in Uniform Flow", performed a series of tests based on the the pseudo-random vibration model developed by Kim Vandiver at MIT using an electromagnetic shaker in the water tunnel. These tests showed a distinct broadening of the response region, both for the oscillating and mean drag coefficients. When compared to results from a mono-component tests with the same input power, Schargel observed a decrease in the mean drag force, and increase in the fluctuating drag force on the randomly vibrating cylinder.

Nakano and Rockwell at Lehigh University have carried out a number of test series of interest to us. These tests were all done at relatively low Reynolds number ($\tilde{1}00$), but allow for interesting qualitative comparisons.

In the first test series,[16] they looked at the effect of frequency modulation on the wake structure. Equation 4.1 gives the form of the input motion $y(t)$. f_e is the nominal excitation frequency, detuned to 95% of the natural shedding frequency for a stationary cylinder. f_m is the modulating frequency and δf_e is the deviation from the excitation frequency, set at 50% for all tests. Varying the ratio f_m/f_e, they found the wake to have a very rich spectral. As seen in Figure 4-1, for rapidly frequency modulated signals, two significant sideband spectral peaks were present. These peaks correspond exactly to locations of the first harmonics of the spectrum of 4.1. [1] At slower frequency modulations they discovered that they could excite a wake that is periodic over a period of $2/f_m$. This mode does not follow directly from the input spectrum, and is a case where the force is not entirely "in phase" with the motion. As the modulating frequency was further decreased, the wake destabilized and a broad peak was present. The peak amplitude of the velocity for the slowly modulating case was less than that for the purely sinusoidal case. The interpretation of a frequency modulated signal as a series of sinuoids, will be important when reconciling the results of the EMD analysis and the power spectrum.

$$y(t) = -Y_e sin\{2\pi f_e t + \delta f_e/f_m sin(2\pi f_e t)\} \tag{4.1}$$

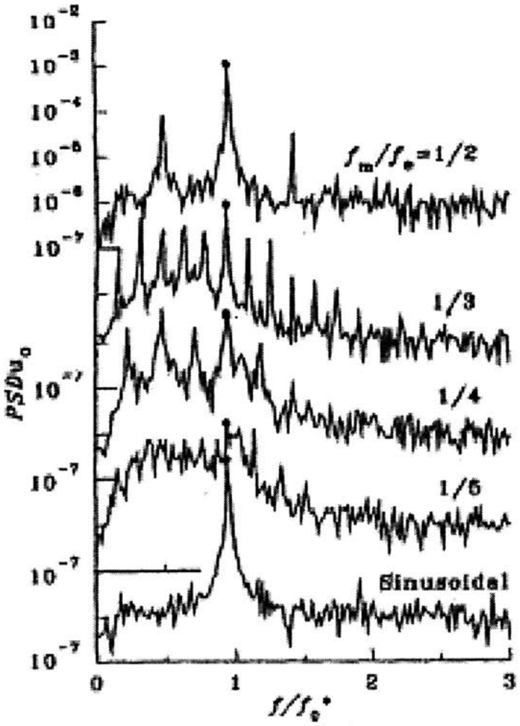

Figure 4-1: Wake Spectra as a function of frequency modulation ratio f_m/f_e

---

[1] The spectrum of a frequency modulated signal consists of a component at f_e and an infinite number of lines at $f_e \pm nf_m$ whose amplitudes are given by Bessel functions.

The second test series by Nakano and Rockwell [17] examines the effect of amplitude modulation on the wake pattern. Their tests showed distinct vortex shedding regimes based on the amplitude of the oscillation and the length of the modulating period compared to the period of excitation. Figure 4-2 shows the states of response of the near-wake reported by Nakano and Rockwell.

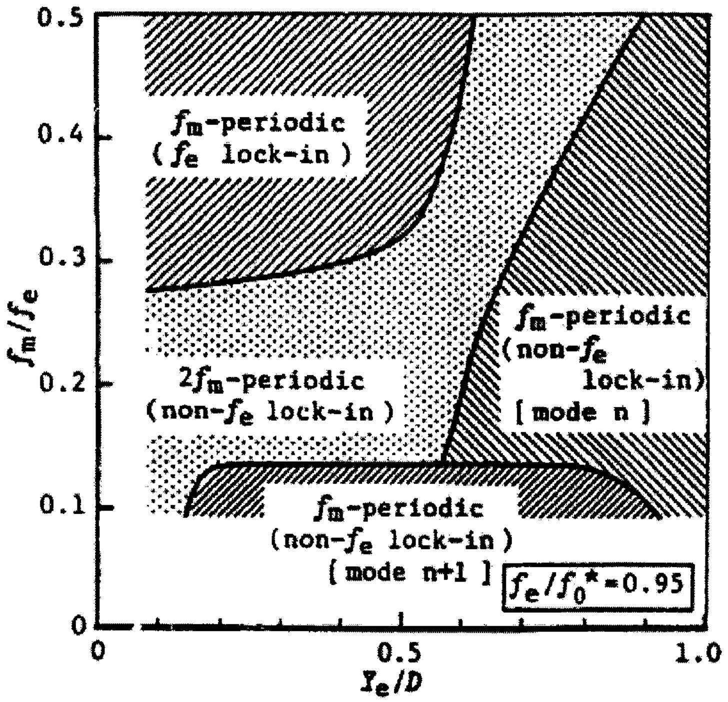

Figure 4-2: Near Wake States, from Nakano and Rockwell [17]

They identified four principal response states

- f_m periodic with f_e lock-in: In this structure, the instantaneous phase of the force/vortex shedding is the same for each f_e cycle. Since this is the case, the wake is also f_m periodic

- f_m periodic with f_e nonlock-in: In this pattern, the instantaneous phase is different from one f_e cycle to the next. However the pattern repeats itself with each envelope.

- $2f_m$ periodic with f_e nonlock-in: Like the above except that the pattern repeats itself everyother 1/fm period

- f_m periodic with f_e nonlock-in (n+1): Differs from pattern two in that an extra pair of vortices are shed with each beat packet.

The equation of amplitude modulated input motion used by Nakano and Rockwell was $y(t) = -(Y_e/2)[1-cos(2\pi f_m)]sin(2\pi f_e t)$ [2]. Like in the frequency modulated set of experiments, Nakano and Rockwell fixed f_e at 95% of the natural shedding frequency and Y_e/D and f_m/f_e was varied. Their principal conclusion was that amplitude modulated motion can produce modulations in the phase angle at which the vortex is shed. States 2-4 are cases where the phase changes from with each $1/f_e$ period. They found that slow beating tended to cause destabilization in the wake, accompanied by a broadening of the wake spectra and decreased peak velocities. On the other hand, phase-locking was observed for fast beating at high A/D's. For fast beats, a model based on the linear superposition of purely sinusoidal results might apply, except that the prescence of the other frequency alters both the phase and amplitude of the forces.

Perhaps the most extensive series of tests on cylinder subjected to beating motions was conducted by Gopalkrishnan at the MIT tow tank. For a variety of modulation ratios and carrier frequencies, Gopalkrishnan looked at the lift forces and phases. These tests pioneered the use of the inner product versions of C_{LV} and C_{LA}. These coefficients are different than C_{LV} and C_{LA} defined at each input frequency, because they do not imply that vortex shedding occurs at the component frequencies, and preserve system power. As seen in Nakano and Rockwell, period doubling and broad band type response can occur due to the amplitude/frequency nature of the oscillation.

Like Nakano and Rockwell Gopalkrishnan observed distinct vortex shedding regimes for both the fast and slow beats. These are shown for beating ratio's of 1:20 and 1:3 in the Figures 4-3 and 4-4. In the modulation ratio 1:N, N refers to the number of excitation cycles per beat packet. Unlike Nakano and Rockwell, Gopalkrishnan witnessed

---

[2] equivalent to a sum of three sinusoids, one at f_e, and at $f_e \pm f_m$

at least some phase modulation for all combinations of modulation ratios and carrier frequencies. In addition periodic phase modulations, where damping and excitation occurs with the envelope of motion, and period doubling, he also observed instances of random phase modulation and frequency switching. In his thesis, Gopalkrishnan also performed an exhaustive series of tests on sinusoidal motions. A comparison of his results to ours is found in the next section.

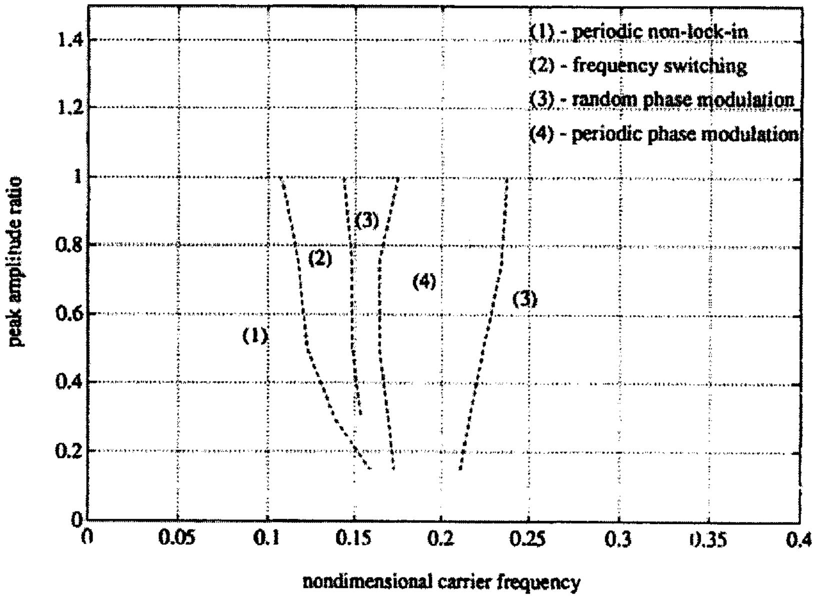

Figure 4-3: Wake response state diagram for 1:20 beats [9]

4.1.2 Mono-Component vibrations

To validate the experimental setup single frequency forced vibration tests were performed. The tests were designed such that we could reproduce to the largest extent possible Gopalkrishnan's results. The tests spanned a reduced frequency range of .05 to .30 at a Reynolds number of 9500. The aspect ratio of the cylinder was 26, compared to 24 for Gopalkrishnan. The principal difference, besides a different apparatus was the use of force sensors at both cylinder supports. The amplitude ratio

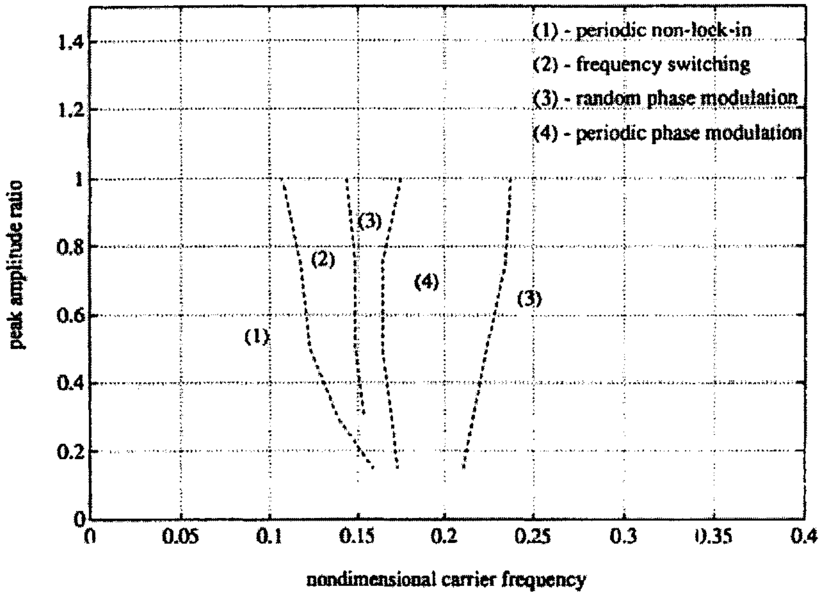

Figure 4-4: Wake response state diagram for 1:3 beats

was chosen to be a moderate .5, which represents the typical maximum A/D ratio seen in the simulations.

Shown in Figure 4-5 is a comparison of the C_{LV} values from the experiment and Gopalkrishnan. These show very similar trends, although there are some marked differences. The peak C_{LV} reached at a $f_r = .175$ is noticeably less than that recorded by Gopalkrishnan. This could be due to a number of factors. As pointed out by Gopalkrishnan, the calculation of C_{LV} is sensitive to the length of the segment over which it is calculated. It is also sensitive to very slight lags in the system, C_{LV} being a linear function at small values of the phase angle. To give an idea of how this translates into real time, for a 1.5hz waveform, a .5 degree shift at 1.5 hz could be caused by less than 1/1000 of a second lag. To avoid amplification of the possible phase lag, we designed our experiments to avoid high frequency oscillations using the VCTA. Per Chapter 2, this meant that testing in the low inflow regions was problematic. Also shown on Figure 4-5 is the C_{LV} computed using the inner product method 3.18. As expected, for a mono-component signal this yields exactly the same

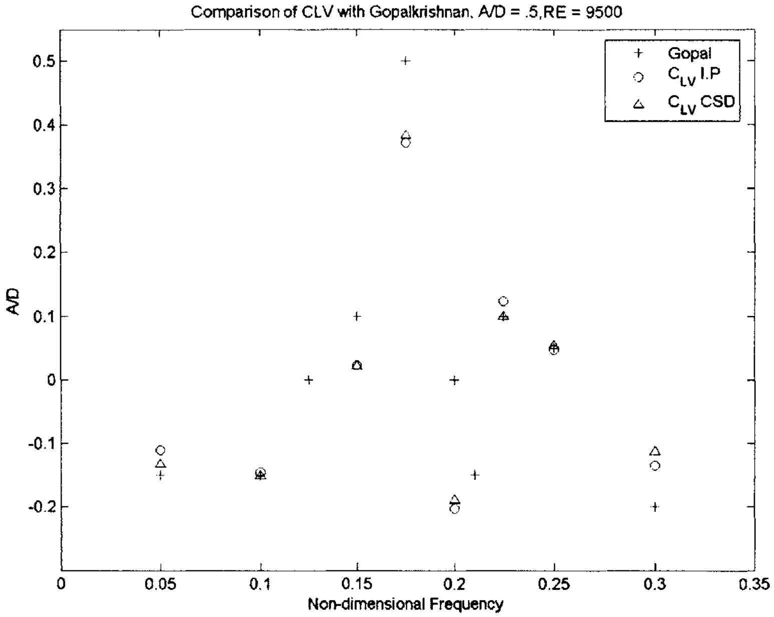

Figure 4-5: Gopalkrishnan C_{LV} for A/D = .5, RE = 9500

result as the CSD method, 3.5.

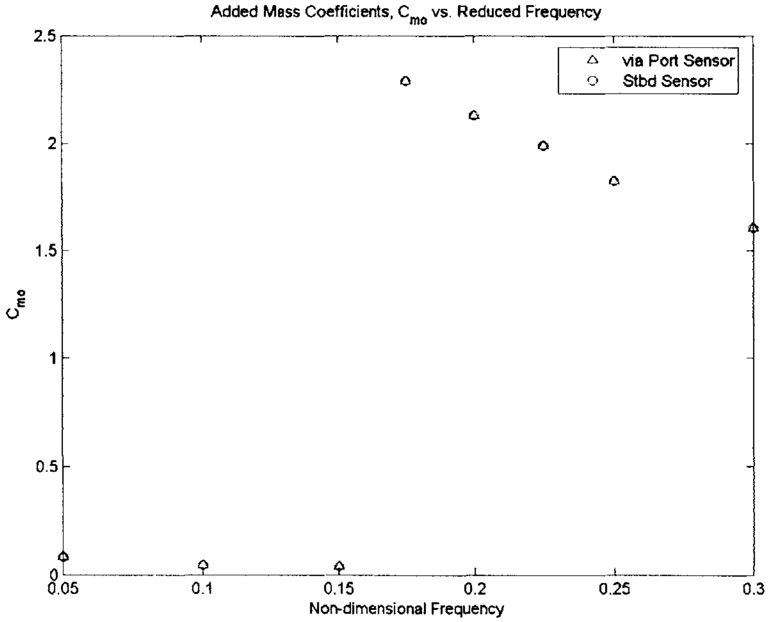

Figure 4-6: C_{Mo} from Port and Starboard Sensors, A/D = .5, RE = 9500

Figure 4-6 contains added mass values calculated separately for the port and starboard force sensors, assuming that each sensor see half the load on the cylinder. We see that the added mass values are virtually identical for the two sensors. The results were also consistent with previous work [15] that showed that correlation between the two ends increases near lock-in.

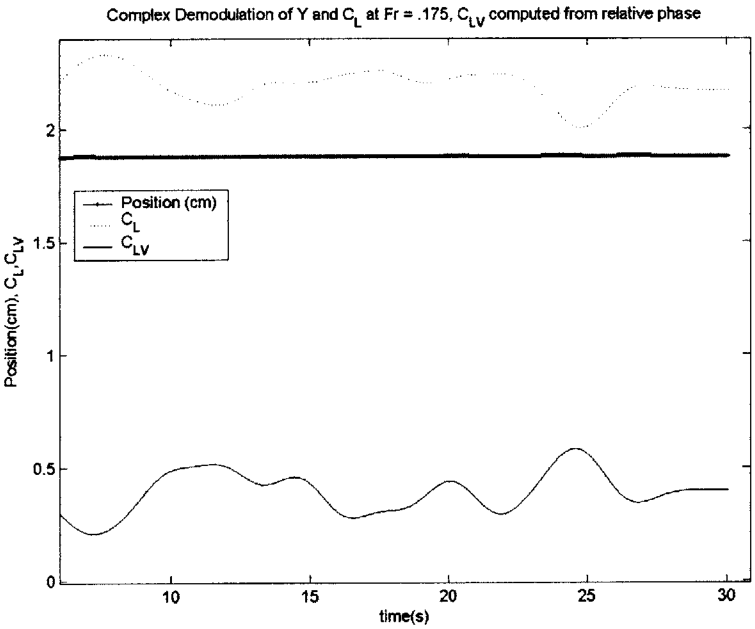

Figure 4-7: $|C_L|$, $|Y|$, and C_{LV} from Complex Demodulation Analysis of A/D = .5, f_r,RE = 9500

Figure 4-7 is the result of the complex demodulation analysis at a reduced frequency of .175. As expected the amplitude from the complex demodulation of the fixed frequency input motion is a constant. Notice that the magnitude of the lift coefficient changes over the course of a run given a fixed input frequency. In addition, notice that C_{LV} fluctuates dramatically and that for portions of the run, it matches the level reported by Gopalkrishnan. One can see clearly that segment choice can influence the value of C_{LV}.

4.1.3 DNS vs. Experiment for Flexible Cylinder in Uniform inflow

Having shown that the experimental set-up can produce results consistent with past experiments, we proceeded with the testing matrix. For the first set of tests, we subjected the cylinder to motions observed at 12 locations along the span of a flexible cylinder in Uniform inflow. The Uniform case was tested first because it didn't require the time/frequency scaling described and thus we could test at locations all along the span. In this sense, the Uniform case was a simple base case. On the other hand, the Uniform case exhibited the most complex response of all the shear flow cases. This was due to the fact that the same structural mode could be excited everywhere along the span. The damping of the energetic modes that typically takes place in the low inflow region could not take place, and waves reflected from the boundaries, setting up standing wave-like patterns in the DNS.

Using the same cylinder as for the mono-component tests, a series a tests were performed at Reynolds Number 7620. The particulars for one of the runs is given in Table 4.1. The position of this test location relative to the boundaries is shown in Figure 4.1.3. The experiment showed high repeatability of the lift force phase. This is consistent with the results of Nakano, that showed that the phase, even if it varied from f_e cycle to f_e cycle, repeated itself for every beat or every other beat. The end force correlation was similarly high. This is consistent with the dominant frequency of the input motion being near the natural shedding frequency.

The input motion and spectra are shown in Figure 4-8. The input spectra contains a narrow peak at a non-dimensional frequency of 0.20, as well as a prominent peak at $f_r = .283$. Table 4.2 contains the values of these peaks as well as the sidelobes of the main peak. It was found that the standard deviation of the position calculated using only the top four frequency was roughly 70% of the actual. Picking out more than 4 peaks, can be problematic as many of them are quite small in amplitude and are often artifacts of the finite data length.

Referring to Figure 4-8, we observe that the magnitude of the DNS C_L (dark

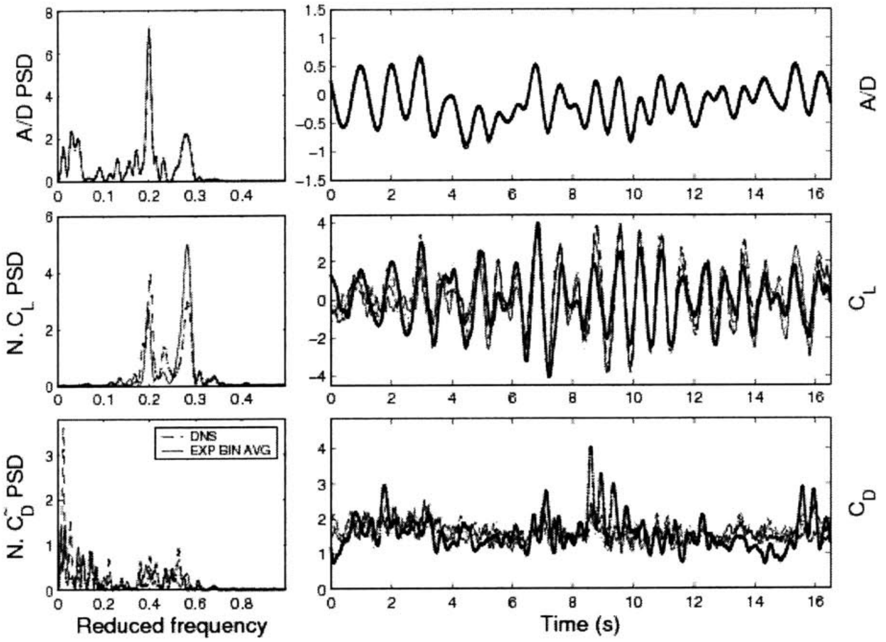

Figure 4-8: Time Series and Spectra for Uniform case, n = 120

line) is slightly greater than the experiment up until 8 seconds, at which point there is a dramatic shift in the peak frequency of the input motion. After this frequency shift, C_{Lexp} dominates for 3 or 4 cycles before the force traces converge again. At the frequency shift the experimental lift leads the DNS by around 10 degrees.

These trends are seen more clearly through complex demodulation in Figure 4.1.3 and in the Hilbert Spectrum 4.1.3. In 4.1.3, we see that the magnitude of C_L at the dominant frequency tapers off for both the experiment and DNS, while at the subdominant frequency it increases as the run progresses, reaching a peak at around 11 seconds. It is interesting to note that $|C_L|$, for the subdominant frequency is almost a linear function of the Y for the experiment. This is to be expected since the acceleration and velocity of the motion, functions of Y, drive the fluid forces. The exact cause of this increase in frequency and the decrease in $|C_{Ldns}|$ is unclear. Complex demodulation is not well suited to capture such a rapid change in phase. The EMD plot, Figure 4.1.3 shows the jump in frequency, however phase information is lost in this representation. The rms C_L is 1.42 for the DNS and 1.49 for the experiment.

Run Particulars	
Shear Profile:	unifl
U_{min}:	1.000 U_{max}
Spanwise Postion:	1901.0 D
Num. of Repeat Tests:	4
Reynolds Number	7620
DNS-Exp. Corr. Score:	90 %
C_L Repeatability:	93.54 %
End Force Corr:	97.19 %
σ of Mean Frequency:	30.66 %
Frequency Resolution:	0.0606 Hz
Exp. C_{LV} via I.P.	0.0282
DNS C_{LV} via I.P.	-0.2406
75 % C.I. $\|C_L\|$, Lower	0.8486
Upper	1.2546

Table 4.1: Run Particulars, Uniform Case

C_{LV} and C_{LA} from the relative phase between force and motion are presented in Figure 4.1.3. The trends mimic those seen in the complex demodulation analysis (CDA) of $|Y|$ and $|C_L|$. The motion at the dominant frequency is damped for the experiment and marginally damped for the simulation. This is not unreasonable considering that we're comparing forced and free vibrations. The C_{LV} for the dominant frequency is slowly varying/periodic, which is consistent for the Gopalkrishnan's wake state of a slowly beating waveform at a carrier frequency of 0.2. The values C_{LV} at the subdominant frequency are similar in form away from the frequency shift at 8 seconds. At the frequency shift C_{LVexp} stays relatively constant. Perhaps this can be explained by considering the jump to be both a rapid change in frequency and amplitude. Recalling Nakano and Rockwell, Figure 4-1, we see that the wake for a rapidly frequency modulated cylinder has distinct frequency components and is nearly phase locked. Gopalkrishnan showed that fast beats at $f_r > .25$ may cause a well behaved modulating phase. Gopalkrishnan surmised that the reason for this may be that the rapid beats don't allow the wake enough time to adjust to the envelope.

The values of C_{LV} from (CDA) agree well with those calculated using the cross-spectrum (see Table 4.2) and the inner product method. The values from the CSD seem to be an average of the value from CDA. Another interesting comparison is to view the fluctuation in the amplitude from CDA as a amplitude modulated motion. Harmonic Analysis shows that for the subdominant frequency this is equivalent to beating at a 1:4.5 modulation ratio. Choosing the peak amplitude ratio to be twice the rms amplitude from CDA, we see that for an equivalent beating waveform at a modulation ration of 1:3, Gopalkrishnan found the C_{LVip} to be around -0.1. This is almost the exact same value as found by the CSD method (Table 4.2, Subdominant 1) or the mean of the CDA time series(Figure 4.1.3).

The added mass values from CDA are shown in 4.1.3. The values of C_{MO} for DNS and Experiment at the dominant frequency are surprisingly similar toward the end of the run, topping out at around 2. An added mass of 2 at a f_r = 0.2, and A/D = 0.23 is slightly lower than the value reported by Gopalkrishnan for a purely sinusoidal experiment. Near the frequency jump the DNS added mass at the subdominant drops to near zero before rising to around 1.25. The added mass from the experiment stays a near constant 1.5 across the frequency shift. The DNS and Experiment values near the end of the run, span the Cm of 1.35 from the contours in Gopalkrishnan's thesis.

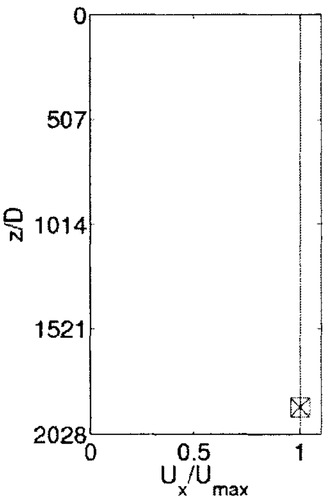

Figure 4-9: Uniform Case, Test Location

C_{LV},C_m, at Peak Frequencies

Frequency	$\frac{fD}{U_x}$	A/D	C_L Coherence	Experiment		Simulation	
				C_{LV}	C_m	C_{LV}	C_m
Dominant	0.2018	0.2303	0.5814	-0.1883	1.2759	-0.2075	1.6911
Subdominant 1	0.2826	0.1342	0.9020	-0.1174	1.6550	-0.2863	1.1470
Subdominant 2	0.1730	0.1115	0.5142	0.0512	0.8621	-0.0134	1.0017
Subdominant 3	0.2163	0.0985	0.6167	-0.2471	0.9854	-0.2240	0.3754

Table 4.2: C_{LV} and C_M at Peak Frequencies, Uniform Case

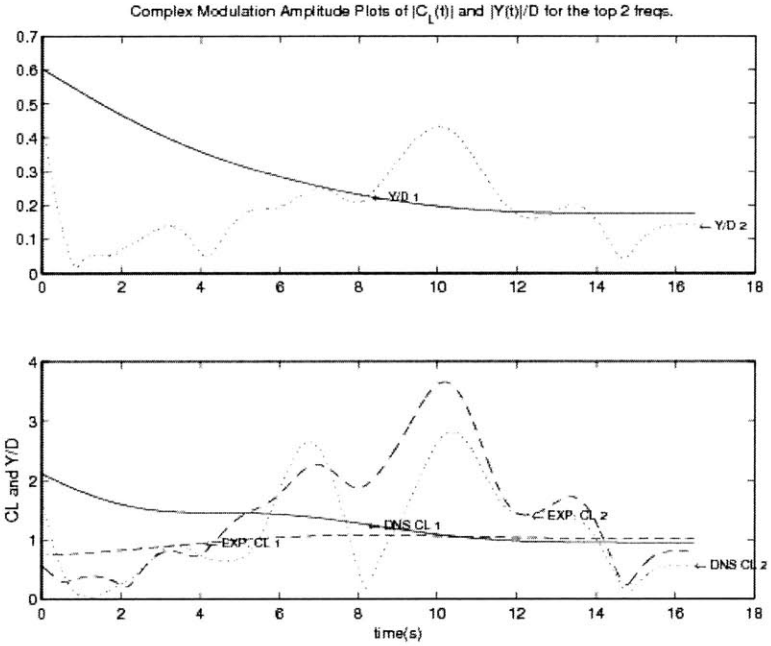

Figure 4-10: Amplitude of motion and C_L for top two frequencies, DNS and Exp., Uniform Case

4.2 Linear Shear Current Profile

The second multi-frequency case tested was for a linear profile with bottom velocity equal to 30% of the maximum velocity. The gradual slope of the profile allowed us to test at equally spaced intervals along 3/4 of the cable's span without exceeding VCTA's capabilities. Results for a low inflow location at 1268 diameters from the upper boundary, and a high inflow location at 317 diameters the are presented.

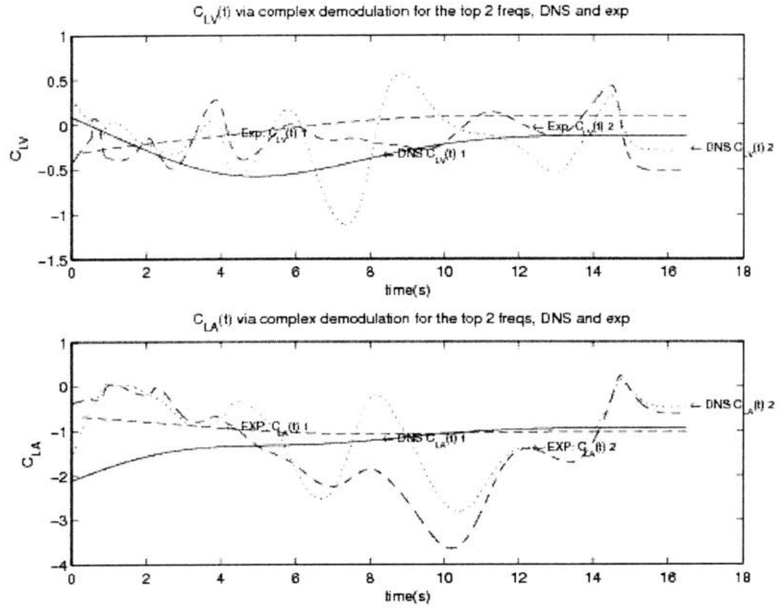

Figure 4-11: $C_{LV}(t)$ and $C_{LA}(t)$ for top two frequencies, DNS and Exp., Uniform Case

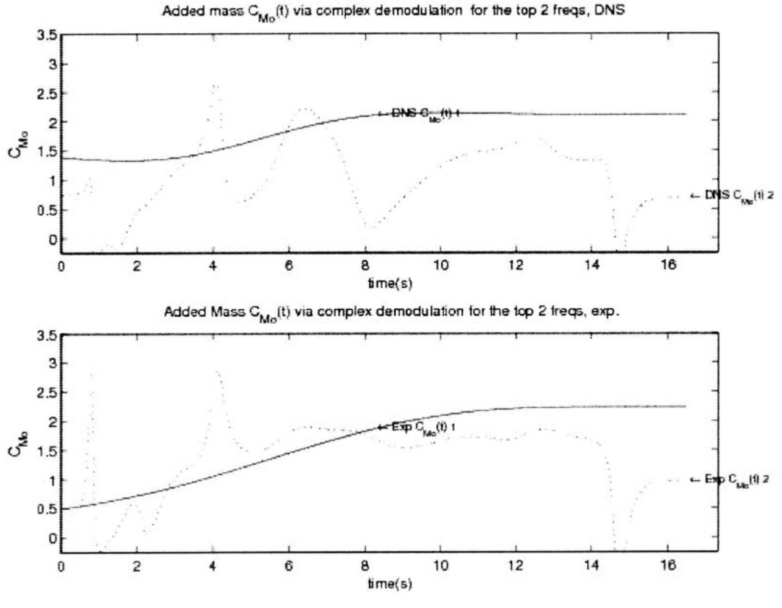

Figure 4-12: Added Mass C_{Mo} for the top two frequencies, DNS and Exp., Uniform Case

4.2.1 Low Inflow Test Location

Particulars for the low inflow case are given in Table 4.5 . The frequency variation in the low inflow region was much lower than that of the Uniform case (on the order

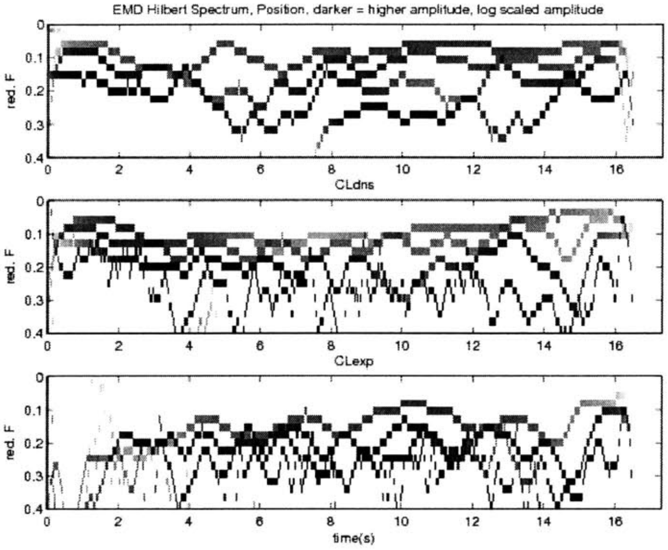

Figure 4-13: EMD Hilbert Spectrum of Y/D and C_L, DNS and Exp.,Uniform Case

of .05% of the mean frequency). Because of this we can infer that fluctuations in the phase and peak broadening are due mostly to amplitude modulation. If we look at the form of the input spectra, it consists of a principal peak at $f_r = 0.38$ and two almost equal sidelobes. This type spectrum is typical of a beating motion, where the frequency of beating is determined by the separation of the sidelobes. This is confirmed upon examination motion time history, where a fast-beating type response is present.

The spectra of the lift force response shows three distinct peaks. The response seems to be almost a linear superposition of the response at each of the component peaks. This behavior is very similar to the "Dual Peak" type response seen by Gopalkrishnan for the fast beating case. If we were to estimate the modulation ratio for this run it would be around 1:6, or between the fast and medium beating cases of Gopalkrishnan. The coherence between the DNS and experiment is high at each of these peaks (see Table 4.4) , meaning that no peak shifts took place.

The lift force time series tells a similar story. The frequency content of the the DNS and the experiment is nearly identical, though the peak magnitude of the lift force is visibly greater. The rms value of the DNS at this location is 2.5 compared to 3 for the experiment. Turning to the complex demodulation plots, Figures 4.2.2 and 4.2.2, We notice that $|C_L|$ for both the experiment and DNS is a nearly a linear function of the motion amplitude. This is a two-dimensional type response. The CDA of C_{LV} shows that damping occurs at the dominant modes, as is expected since the cable is being excited in the high inflow region. This may be one the reasons for the similarities between the forced experiment and free vibration experiment; the cylinder in the DNS is essentially being forced by the structure at this location. The C_{LV} for both modes is slowly varying and scaling with the motion amplitude. More significant damping occurs near the middle of the run in the DNS, resulting in slightly lower CSD values of C_{LV} for the DNS (see Table 4.4). One should be careful in interpreting the first 3 seconds of the CDA as a little ringing occurs due to the low pass filter's initial condition.

The CDA of C_{LA} shows trends similar to those observed for C_{LV}. Namely, the the shape of the curves is are nearly identical, with an offset due to the difference in lift force magnitude. Likewise the C_{Mo} for the DNS and Experiment are very similar, with a higher added mass for the subdominant frequency near the middle of the run. The mean values of C_{mo} for both modes in the experiment is around 1.5. The mean value for the DNS is 1.2. The difference between the two is equal to the difference in the rms values. The same values are found in Table 4.4, using the CSD method. At this location, the 2-d experiment closely captures the 3-d behavior of the DNS.

4.2.2 High Inflow Test Location

Results from the same set of tests but at a region of high inflow region are given below. In this test the inflow velocity represented about 90% of maximum inflow velocity as compared to 55% for the case previously discussed. Like the uniform case, the cylinder in the linear current at high inflow exhibit very intricate motions. Looking at Figure 4-19 we see that there is a low frequency component to the motion as well as a series of beats of irregular length. The motion spectra is comprised of two narrow peaks just above the natural shedding frequency, and a peak at an $f_r = .26$.

The lift force traces show that there are distinct regions where the phases and magnitudes of the lift coefficients are similar and regions where they diverge. Using a moving window it was estimated that the DNS and experiment show higher than 50% correlation for 70% of the run. We can also see that for the first half of the run, the experimental lift force is significantly greater than the DNS, while between t = 15-20 the DNS lift exceeds the experimental values. This results in rms values of 1.34 for the DNS lift coefficient and 1.63 for the experiment. The spectrum of the lift force is slightly broader than the input spectrum, as indicated by Nakano and Rockwell, and Gopalkrishnan, this is due to the destabilizing effect of the slow amplitude modulations seen in the $|Y|$ from CDA (Figure 4.2.2) and in the modulations of motion frequency seen in the Hilbert Spectrum (Figure 4.2.2).

Around 10 seconds, we can see that the DNS lift force leads the experimental lift by around 10 degrees. If we look at the CDA of the C_{LV}, we see that there is a substantial positive C_{LV} for both modes at this instance. Like the frequency shift in the Uniform case, this jump is most likely due to three-dimensional effects, but is difficult to pinpoint the cause. A clue is given in the EMD analysis (Figure 4.2.2) where the mean frequency of oscillation decreases to $f_r = .15$ before t = 10 and then increases to a $f_r = .3$ before decreasing again to a f_r of .21. A possible explanation might be that if the decrease in frequency was caused by the surrounding structure, and the wake were still tuned to the dominant frequency then we would see a substantial positive C_{LV}. This C_{LV} could excite the structure leading to an increase in frequency. However at some point the wake structure would catch up and significant damping would occur at the higher frequency, at which point the frequency would decrease and return to a state near the natural frequency of shedding. Questions such as this arise in almost every high inflow case and are difficult/impossible to answer without wake visualization.

On the whole, we see fairly extreme changes in C_{LV} occurring in the 3-dimensional case, while for the experiment there is a slightly negative C_{LV} for its duration. Viewing the amplitude from CDA at the peak frequency as a beating waveform with modulation ratio 1:12, we see that a marginally damped response is what we'd expect given the experiments of Gopalkrishnan.

Away from the region with the phase shift, the C_{LA} values from Experiment and DNS show similar trends, though they only approach similar values toward the end of the run. At the end of the run, the added mass values for the dominant mode is around 2.1 for DNS and 1.8 for the experiment. The added mass at the subdominant frequency is around 1.7 both the experiment and DNS. Near the phase shift the added mass of the DNS behaves erratically.

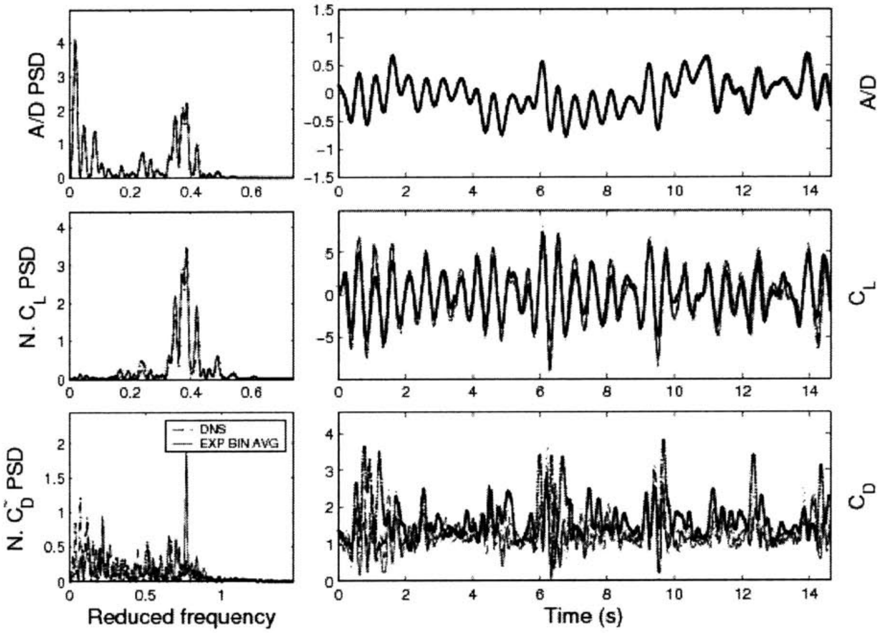

Figure 4-14: Time Series and Spectra for Linear case, Low Inflow

4.3 Summary of Results

The results from representative cases are mirrored to a large extent in all the shear flow profiles tested. Moving along the cylinder span, the correlation between the 2-d experiment and the DNS typically increases as the local inflow velocity decreases relative to the maximum inflow velocity. Figure 1-12, shows the cross-over between fluid forcing for a number of shear cases. After the mean C_{LV} changes from positive to negative, we begin to see less frequent frequency shifts such as described in subsections 4.1.3 and 4.2.2. For convenience the region from the maximum velocity to the cross-

Run Particulars	
Shear Profile:	lin2
U_{min}:	0.522 U_{max}
Spanwise Postion:	1268.0 D
Num. of Repeat Tests:	4
Reynolds Number	7620
DNS-Exp. Corr. Score:	98.00 %
C_L Repeatability:	97.59 %
End Force Corr:	97.86 %
σ of Mean Frequency:	0.03 %
Frequency Resolution:	0.0684 Hz
Exp. C_{LV} via I.P.	-0.2359
DNS C_{LV} via I.P.	-0.4272
75 % C.I. $\|C_L\|$, Lower	0.8486
Upper	1.2546

Table 4.3: Run Particulars for Linear Case, Low Inflow

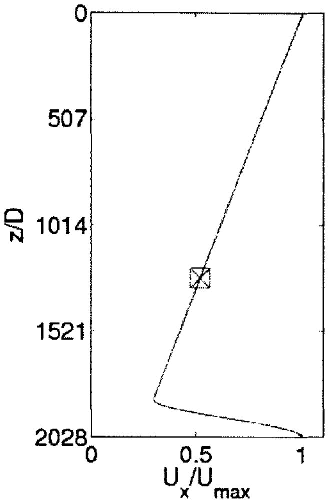

Figure 4-15: Linear Case, Low Inflow, Test Location

over we'll denote "High Inflow" and from the cross-over onward "Low Inflow".

High Inflow The high inflow region is characterized by vibration at or slightly above the local natural shedding frequency. In this region the response can be both frequency and amplitude modulated. In all the cases tested, the RMS 2-d lift force was equal to or greater than the RMS of the 3-dimensional DNS, so in one sense, the 2-d Lift force is conservative. However, we found that instantaneously the C_{LV} can vary wildly in the DNS, and assume values far exceeding the exper-

C_{LV},C_m, at Peak Frequencies

Frequency	$\frac{fD}{U_x}$	A/D	C_L Coherence	Experiment		Simulation	
				C_{LV}	C_m	C_{LV}	C_m
Dominant	0.3893	0.1391	0.9664	-0.1470	1.4916	-0.2873	1.2014
Subdominant 1	0.3749	0.1329	0.9709	-0.1042	1.5182	-0.1049	1.2016
Subdominant 2	0.3518	0.1241	0.9760	-0.0927	1.6312	-0.0182	1.1019
Subdominant 3	0.4210	0.0961	0.9444	-0.0639	1.5040	-0.1062	1.1109

Table 4.4: C_{LV} and C_M at Peak Frequencies, Linear Case, Low Inflow

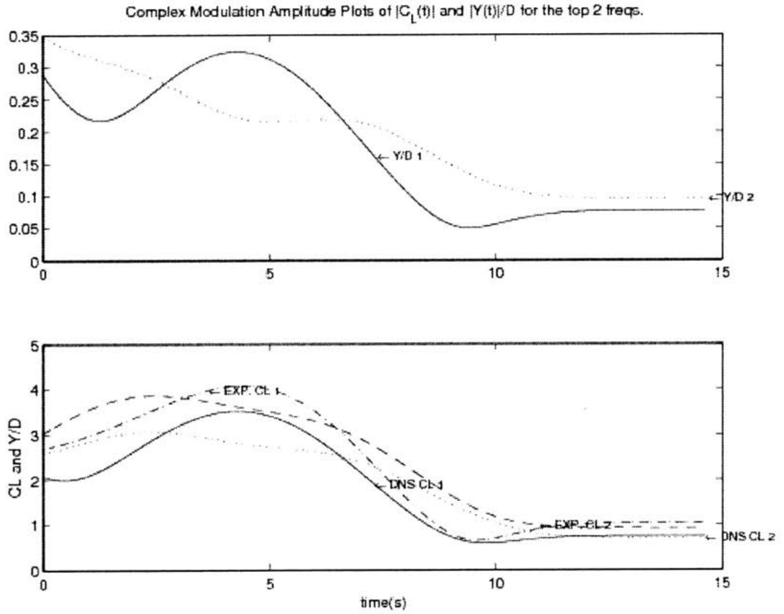

Figure 4-16: Amplitude of motion and C_L for top two frequencies, DNS and Exp., Linear Case, Low Inflow

imental values or values from equivalent beating waveforms in Gopalkrishnan. Luckily, this behavior seems to be self-regulating, and often instances of high excitation are followed by high damping. Furthermore, the DNS lift coefficient at these instances was observed to be less than the 2-dimensional experiment. Further study of the mechanisms behind these phase variations is required. Away from segments of the time series where these rapid phase changes take place, the 2-dimensional experiment captured the 3-d behavior reasonably well. It was seen that the added mass values are often very close, with the experi-

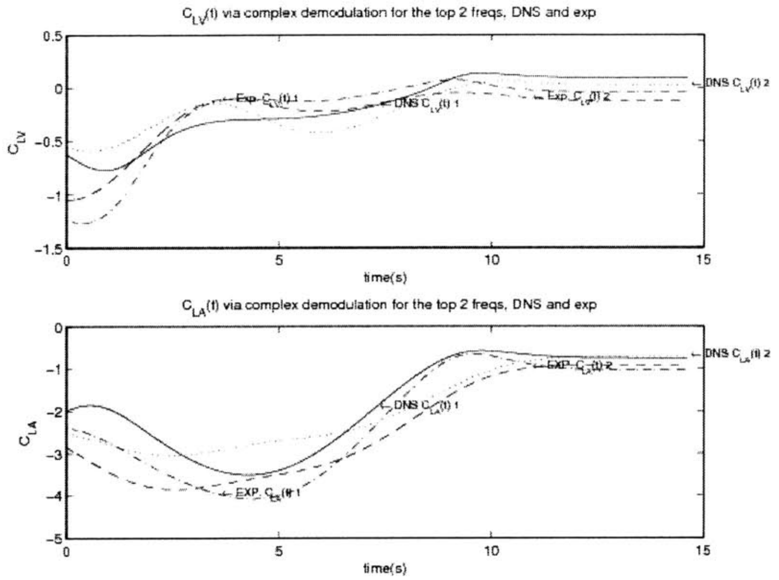

Figure 4-17: $C_{LV}(t)$ and $C_{LA}(t)$ for top two frequencies, DNS and Exp., Linear Case, Low Inflow

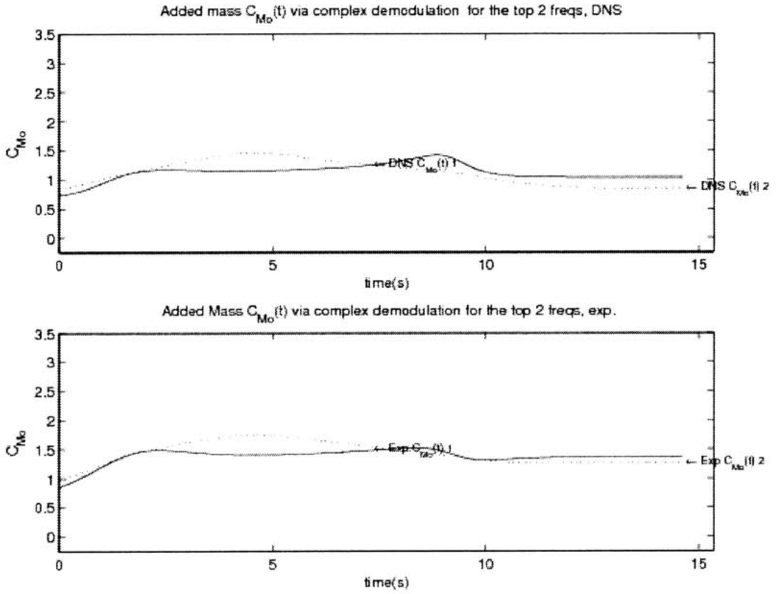

Figure 4-18: Added Mass C_{Mo} for the top two frequencies, DNS and Exp., Linear Case, Low Inflow

ment tending to produce slightly higher values. However, these differences may be the results of a a bias in the experiment. For if we compare Figure 4-6 to

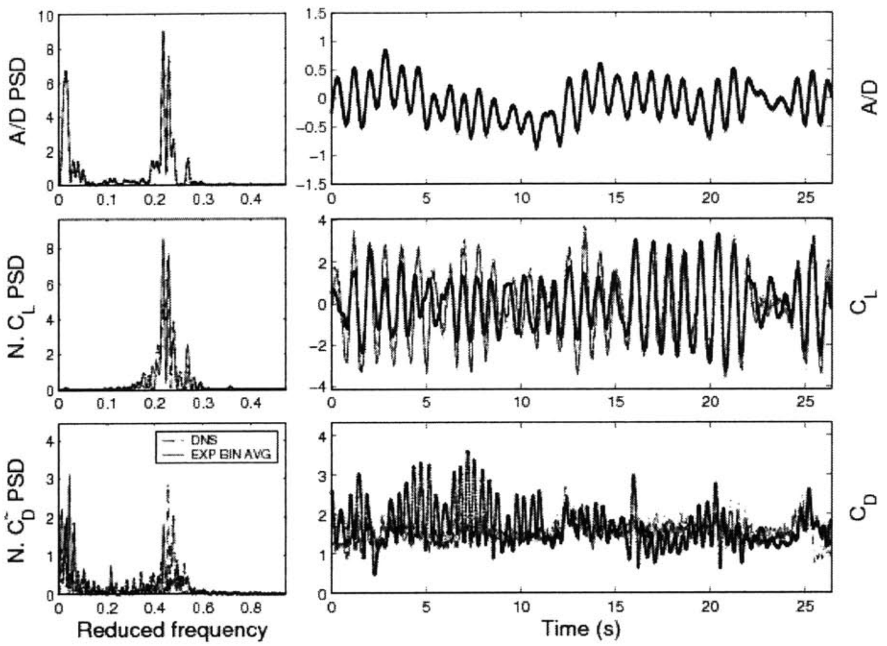

Figure 4-19: Time Series and Spectra for Linear case, High Inflow

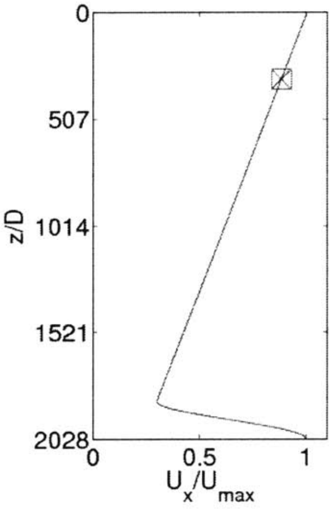

Figure 4-20: Test Location, Linear Case, Low Inflow

values from Gopalkrishnan for the same force vibration experiment, we see that our added mass values are about 20% higher. Further testing would alleviate this uncertainty. There were some discrepancies in the C_{LV} between the DNS and experiment, even away from the rapid phase changes. More often than

Run Particulars	
Shear Profile:	lin2
U_{min}:	0.885 U_{max}
Spanwise Postion:	317.0 D
Num. of Repeat Tests:	3
Reynolds Number	7620
DNS-Exp. Corr. Score:	70 %
C_L Repeatability:	98.42 %
End Force Corr:	94.97 %
σ of Mean Frequency:	13.79 %
Frequency Resolution:	0.0379 Hz
Exp. C_{LV} via I.P.	-0.0748
DNS C_{LV} via I.P.	0.0213
75 % C.I. $\|C_L\|$, Lower	0.8332
Upper	1.3014

Table 4.5: Run Particulars for Linear Case,high Inflow

C_{LV},C_m, at Peak Frequencies

Frequency	$\frac{fD}{U_x}$	A/D	C_L Coherence	Experiment		Simulation	
				C_{LV}	C_m	C_{LV}	C_m
Dominant	0.2191	0.2132	0.6354	-0.0220	2.0061	-0.4757	0.8871
Subdominant 1	0.2307	0.1944	0.6528	-0.0421	1.8923	-0.0071	0.9477
Subdominant 2	0.2408	0.1121	0.6501	-0.0024	1.9273	0.2994	1.3611
Subdominant 3	0.2696	0.0900	0.5470	-0.1155	1.7051	-0.0717	1.0573

Table 4.6: C_{LV} and C_M at Peak Frequencies, Linear Case, High Inflow

not, the trend was for the experimental lift force to dampen the motion. These discrepancies are probably attributable to differences between a forced and free vibration experiment.

Low Inflow The low inflow region is characterized by vibration above the natural shedding frequency based on the local inflow velocity. In this region we saw a high correlation between the DNS and experimental lift forces. Time frequency analysis showed that in this region the signal is more stationary and often forms coherent beat packets. For these cases, C_{LV} and C_M were found to modulate slowly over the course of the run. This is consistent with the phase modulation observed by Gopalkrishnan for beating waveform with $f_r > .2$.

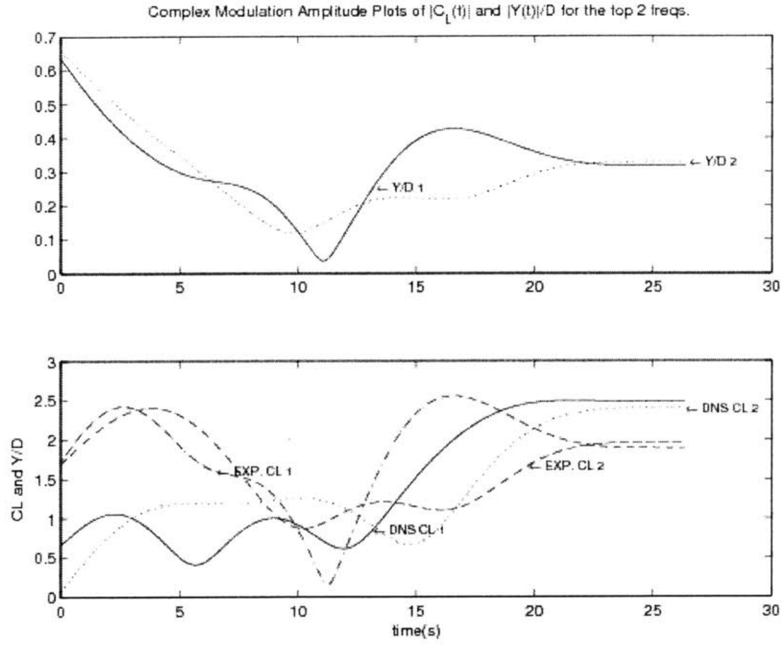

Figure 4-21: Amplitude of motion and C_L for top two frequencies, DNS and Exp., Linear Case, High Inflow

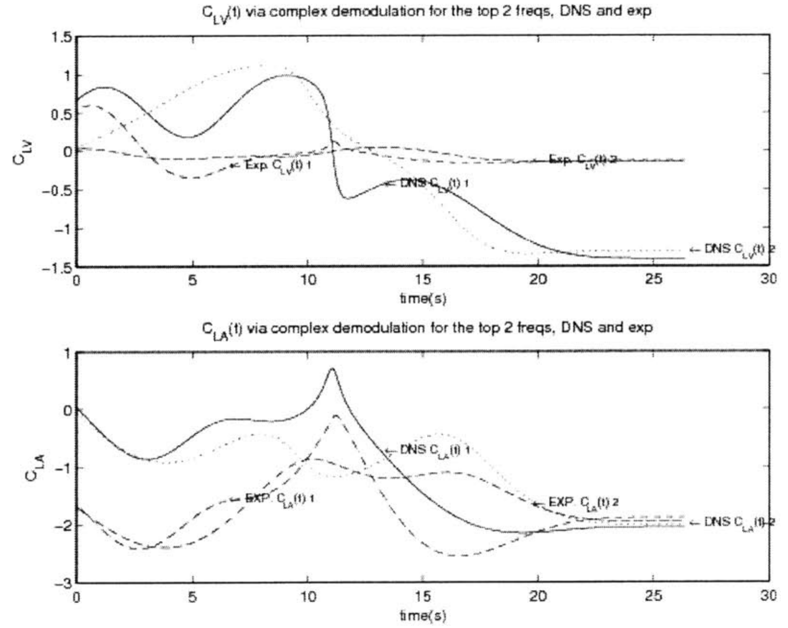

Figure 4-22: $C_{LV}(t)$ and $C_{LA}(t)$ for top two frequencies, DNS and Exp., Linear Case, High Inflow

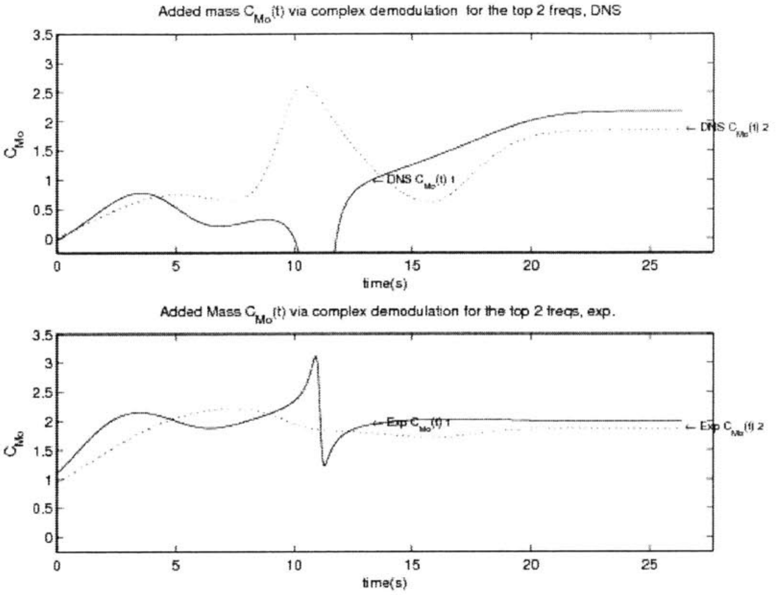

Figure 4-23: Added Mass C_{Mo} for the top two frequencies, DNS and Exp., Linear Case, High Inflow

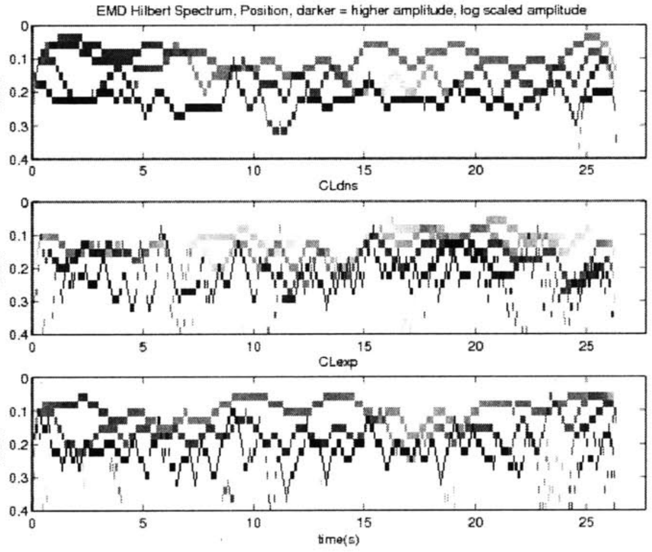

Figure 4-24: EMD Hilbert Spectrum of Y/D and C_L, DNS and Exp., Linear Case, High Inflow

4.4 Hydrodynamic Force Modeling

A logical approach to modeling the hydrodynamic force is to consider the forcing to be a sum of N sinusoids in the form of Equation 3.1. Using the CSD method or the average of the values from CDA we can easily find the amplitude and phase of each of the sinusoids. For our experiments it was found that we could usually only distinguish four physical peaks containing significant energy. Peaks below this level were often artifacts from windowing. Tables 4.7, 4.8 and 4.9, column 1, contains the RMS value of the input motion if we consider only frequency component 1:i, divided by the actual RMS value of the motion, for the three cases discussed. We see that a model considering only the dominant frequency captures only 0.50 of the rms value of the input motion(or 0.25 of the energy). A model considering the top four would contain around 0.42 of the total signal energy. The same thing can be done with the components of the lift force at the peak input frequencies. A four frequency model's based on the experiment and the DNS captures about 0.50. As seen in Table 4.8 at low inflow locations, these models do a little better. However for all finite frequency models, some energy is lost due to the fairly wide band nature of the input motion and the spreading effect that frequency and amplitude modulation has on the lift spectrum.

It was for this reason that Gopalkrishnan adopted the inner product forms of C_{LV} and C_{LA} for these preserve signal energy. The difficulty arises however in determining a characteristic amplitude and motion to describe the coefficient. The simplest option is to look at the modulation of the motion amplitude as seen in Figure 4.4 and from harmonic analysis find the mean frequency of the modulation. In this case the modulation ratio of mean frequency modulation frequency to the mean excitation frequency is around 1:4, or rather rapidly modulated. As a comparison, we calculated a C_{LV} of roughly 0 for the Uniform case, with a equivalent peak amplitude ratio of 0.66 (for a waveform RMS matched with Gopalkrishnan, the peak amplitude ratio is twice the RMS value). For this RMS matched waveform, Gopalkrishnan found a C_{LV} of .3 and a C_{LA} of 1.5, giving a rms of value of 1.53 for C_L. This compares favorably to the value of 1.49 computed for the waveform. However, its utility is diminished considerably since the power transfer was incorrectly predicted.

Another option would be look at the amplitude from complex demodulation at the peak frequencies to find the equivalent beating motion. The difficulty in this, or

Frequency	f(i)	$\sigma_{Y_{1:i}}/\sigma_Y$ based on $Y_{f(1:i)}$	$\sigma_{CLdns_{1:i}}/\sigma_{CLdns}$ based on $CLdns_{f(1:i)}$	$\sigma_{CLexp_{1:i}}/\sigma_{CLexp}$ based on $CLexp_{f(1:i)}$
Dominant	0.2018	0.4889	0.3574	0.5081
Subdominant 1	0.2826	0.5659	0.6831	0.6716
Subdominant 2	0.1730	0.6134	0.6928	0.6783
Subdominant 3	0.2163	0.6481	0.7093	0.6956

Table 4.7: Uniform Case, RMS values of lift and motion for a four frequency model

Frequency	f(i)	$\sigma_{Y_{1:i}}/\sigma_Y$ based on $Y_{f(1:i)}$	$\sigma_{CLdns_{1:i}}/\sigma_{CLdns}$ based on $CLdns_{f(1:i)}$	$\sigma_{CLexp_{1:i}}/\sigma_{CLexp}$ based on $CLexp_{f(1:i)}$
Dominant	0.3893	0.3189	0.3683	0.4505
Subdominant 1	0.3749	0.4410	0.5294	0.6132
Subdominant 2	0.3518	0.5248	0.6527	0.6887
Subdominant 3	0.4210	0.5692	0.7602	0.7625

Table 4.8: Linear Case, Low Inflow, RMS values of lift and motion for a four frequency model

any linear superposition type of model is that the presence of the other frequency component influences the lift and phase of the other frequency components. To be able to use this kind of method you would need to have a way of determining the sensitivity of one frequency component to another.

Assigning an semi-arbitrary beating waveform to a complex signal might be foolhardy, for as we saw in the complex demodulation plots for the high inflow case, the beating patterns are rarely periodic. To properly account for the effect of multiple frequency components might will require additional work. These experiments and the DNS simulations constitute a first step.

Frequency	f(i)	$\sigma_{Y_{1:i}}/\sigma_Y$ based on $Y_{f(1:i)}$	$\sigma_{CLdns_{1:i}}/\sigma_{CLdns}$ based on $CLdns_{f(1:i)}$	$\sigma_{CLexp_{1:i}}/\sigma_{CLexp}$ based on $CLexp_{f(1:i)}$
Dominant	0.2191	0.4602	0.5101	0.4144
Subdominant 1	0.2307	0.6228	0.7049	0.5344
Subdominant 2	0.2408	0.6682	0.7649	0.6414
Subdominant 3	0.2696	0.6959	0.8176	0.6792

Table 4.9: Linear Case, High Inflow, RMS values of lift and motion for a four frequency model

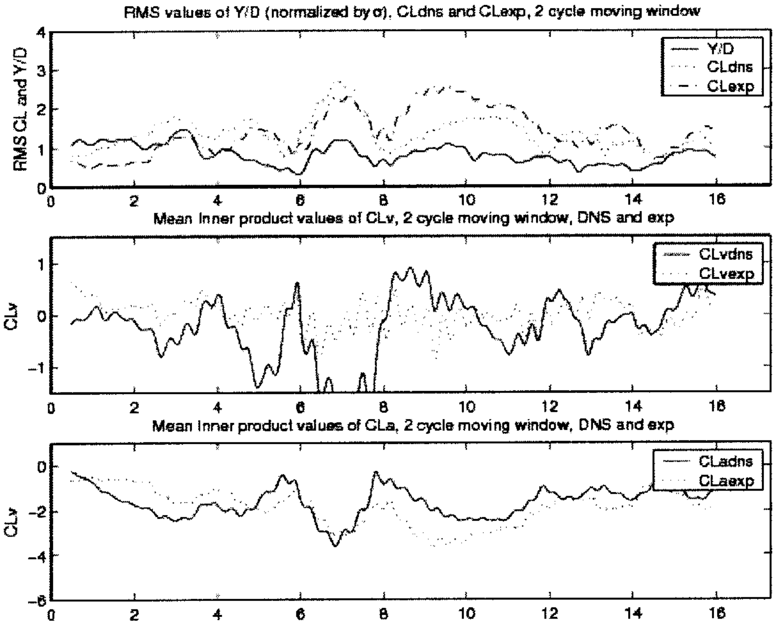

Figure 4-25: RMS values of Y and C_L, 2 Cycle moving window, DNS and Exp., Uniform Case

Chapter 5

Future Work

In addition to additional testing and thorough analysis of the drag, there are a number of natural "next steps" in furthering our understanding of multi-frequency cylinder vibrations.

- Extend capabilities in the tow tank or propeller tunnel to higher Reynolds number. To reach full-scale type Reynolds numbers (100,000+) this would require an electro-hydraulic system to meet the high frequency/long stroke programmable requirements.

- Perform flow visualization comparisons between the DNS and the experiment.

- Development of a set of parameters that could indicate where, and when strip theory won't apply.

- Perform a critical review of Time/Frequency tools such as wavelets, EMD and the Wigner distributions such that we may be able to accurately quantify the non-stationary behavior in the high inflow region.

- Once we have an understanding of the frequency modulations present in the DNS, perform a set of experiments with frequency modulation at higher Reynolds number than Nakano and Rockwell. This coupled with the beating results given in Gopalkrishnan could provide a good basis for a hydrodynamics force model.

- Synthesize the results of the DNS, these experiments, and ones on frequency modulation into an improved hydrodynamic force model for VIV.

Bibliography

[1] R. Blevins. *Flow-Induced Vibration.* Van Nostrand Reinhold Company, New York, New York, second edition, 1990.

[2] P. Bloomfield. *Fourier Analysis of Time Series: An Introduction.* Wiley Series in Probability and Statistics. John Wiley and Sons, New York, NY, second edition, 2000.

[3] B. Boashash, editor. *Time Frequency Signal Analysis and Processing: A Comprehensive Reference.* Elvesier, Oxford,UK, first edition, 2003.

[4] T. Y. Chung. *Vortex-Induced Vibration of Cylinders in Sheared Flows.* PhD dissertation, Massachusetts Institute of Technology, Department of Ocean Engineering, 1987.

[5] J. Davis, F. Hover, and M. S. Triantafyllou. Three-dimensionality of mode transition in vortex-induced vibrations of a circular cylinder. *European Journal of Mechanics - B/Fluids*, 23:29–40, 2004.

[6] S. Dong and G. E. Karniadakis. DNS of flow past a stationary and oscillating rigid cylinder at RE = 10,000. In *Proceedings Flow Induced Vibrations*, Ecole Polytechnique, Paris, July 2004.

[7] P. Esquef, V. Vlimki, K. Roth, and I. Kauppinen. Interpolation of long gaps in audio signals using the warped burg's method. In *Proc. 6th Int. Conf. Digital Audio Effects (DAFx-03)*, pages 18–23, London,UK, September 2003.

[8] C. Evangelinos, D. Lucor, L. Imas, and G. E. Karniadakis. Flow-induced vibrations of non-linear cables. Part 2: Simulations. *International Journal for Numerical Methods in Engineering*, 55(5):557–571, 2002.

[9] R. Gopalkrishnan. *Vortex Induced Forces on Oscillating Bluff Cylinders.* PhD dissertation, Massachusetts Institute of Technology, Department of Ocean Engineering, 1993.

[10] N. E. Huang, Z. Shen, S. R. Long, M. C. Wu, and E. H. Shih. The empirical mode decomposition method and the hilbert spectrum for non-stationary time series analysis. *Proc. Roy. Soc. London*, A454:903–995, 1998.

[11] K. E. Kaasen, H. Lie, F. Solaas, K. Vandiver, and J. Kim. Analysis of vortex-induced vibrations of marine risers based on full-scale measurements. In *Offshore Technology Conference*, Houston, Texas, April 2000.

[12] S. Krishnanmoorthy, S. J. Price, and M. P. Paidoussis. Cross-flow past and oscillating circular cylinder: synchronization phenomena in the near wake. *Journal of Fluids and Structures*, 15:955–980, October 2001.

[13] D. Lucor, L. Imas, and G. Karniadakis. Vortex dislocations and force distribution of long flexible cylinders subjected to sheared flows. *Journal of Fluids and Structures*, 15:641–650, April 2001.

[14] D. Lucor, X. Ma, M. S. Triantafyllou, and G. E. Karniadakis. Vortex-induced vibrations on long marine risers in sheared flows: DNS studies. In *Proc. 4th ASME/JSME Joint Fluids Engineering Conference*, Honolulu, Hawaii, July 2003. ASME/JSME.

[15] S. Miller, F. Hover, and M. S. Triantafyllou. Vortex-induced vibration of marine cables: experiments using force feedback. *Journal of Fluids and Structures*, 11:307–326, April 1997.

[16] M. Nakano and D. Rockwell. Destabilization of the karman vortex street by frequency-modulated excitation. *Physics of Fluids*, 3:723–725, 1991.

[17] M. Nakano and D. Rockwell. The wake from a cylinder subjected to amplitude-modulated excitation. *Journal of Fluid Mechanics*, 247:79–110, 1993.

[18] A. Papoulis. A new algorithm in spectra analysis and band-limited signal extrapolation. *IEEE trans. Circuits Syst*, CAS-22:735–742, Sept. 1975.

[19] T. Sarpkaya. Force on a circular cylinder in viscous oscillatory flow at low keulegan-carpenter numbers. *Journal of Fluids Mechanics*, 195:61–71, 1986.

[20] T. Sarpkaya. A critical review of the intrinsic nature of vortex-induced vibrations. *Journal of Fluids and Structures*, 19:389–447, May 2004.

[21] R. Schargel. The drag coefficient for a randomnly oscillating cylinder in a uniform flow. Master's thesis, Massachusetts Institute of Technology, Department of Ocean Engineering, 1980.

[22] O. Smogeli. Design and evaluation of a force-feedback control system for viv experiments. Master's thesis, Massachusetts Institute of Technology, Department of Ocean Engineering, 2002.

[23] A. Techet, F. Hover, and M. S. Triantafyllou. Forces on oscillating uniform and tapered cylinders in crossflow. *Journal of Fluids Mechanics*, 363:97–114, May 1998.

[24] A. Techet, F. Hover, and M. S. Triantafyllou. Vortical patterns behind a tapered cylinder oscillating transversely to a uniform flow. *Journal of Fluids Mechanics*, 363:79–96, May 1998.

[25] C. Williamson and R. Govardhan. Vortex-induced vibrations. *Annual Review of Fluid Mechanics*, 36(1):413–455, 2004.

[26] C. Williamson and A. Roshko. Vortex-formation in the wake of an oscillating cylinder. *Journal of Fluids and Structures*, 2:355–381, 1988.

[27] N. Wu. *The Maximum Entropy Method.* Springer Series in Information Sciences. Springer-Verlag, Berlin, first edition, 1997.